CHAOS VIII: Far-Ultraviolet Spectra of M101 and The Impact of Wolf-Rayet Stars*

Danielle A. Berg, ¹ Evan D. Skillman, ² John Chisholm, ¹ Richard W. Pogge, ^{3,4} Simon Gazagnes, ¹ Noah S. J. Rogers, ^{5,6} Dawn K. Erb, ⁷ Karla Z. Arellano-Córdova, ⁸ Claus Leitherer, ⁹ Jackie Appel, ¹⁰ and John Moustakas ¹¹

¹Department of Astronomy, The University of Texas at Austin, 2515 Speedway, Stop C1400, Austin, TX 78712, USA

²Minnesota Institute for Astrophysics, University of Minnesota, 116 Church St. SE, Minneapolis, MN 55455

³Department of Astronomy, The Ohio State University, 140 W 18th Ave., Columbus, OH, 43210

⁴Center for Cosmology & AstroParticle Physics, The Ohio State University, 191 West Woodruff Avenue, Columbus, OH 43210

⁵Department of Physics and Astronomy, Northwestern University, 2145 Sheridan Road, Evanston, IL 60208, USA

⁶Center for Interdisciplinary Exploration and Research in Astrophysics (CIERA), Northwestern University, 1800 Sherman Avenue, Evanston, IL 60201, USA

⁷Center for Gravitation, Cosmology and Astrophysics, Department of Physics, University of Wisconsin Milwaukee, 3135 N Maryland Ave., Milwaukee, WI 53211, USA

8 Institute for Astronomy, University of Edinburgh, Royal Observatory, Edinburgh, EH9 3HJ, UK
 9 Space Telescope Science Institute, 3700 San Martin Drive, Baltimore, MD 21218, USA
 10 Associate News Editor, Popular Mechanics Magazine
 11 Department of Physics & Astronomy, Siena College, 515 Loudon Road, Loudonville, NY 12211

ABSTRACT

We investigate the stellar and nebular properties of 9 H II regions in the spiral galaxy M101 with far-ultraviolet (FUV; $\sim 900-2000$ Å) and optical ($\sim 3200-10000$ Å) spectra. We detect significant C III] $\lambda\lambda1907,1909$ nebular emission in 7 regions, but O III] $\lambda1666$ only in the lowest-metallicity region. We produce new analytic functions of the carbon ICF as a function of metallicity in order to perform a preliminary C/O abundance analysis. The FUV spectra also contain numerous stellar emission and P-Cygni features that we fit with luminosity-weighted combinations of single-burst Starburst99 and BPASS models. We find that the best-fit Starburst99 models closely match the observed very-high-ionization P-Cygni features, requiring very-hot, young ($\lesssim 3$ Myr), metal-enriched massive stars. The youngest stellar populations are strongly correlated with broad He II emission, nitrogen Wolf-Rayet (WR) FUV and optical spectral features, and enhanced N/O gas abundances. Thus, the short-lived WR phase may be driving excess emission in several N P-Cygni wind features ($\lambda955$, $\lambda991$, $\lambda1720$) that bias the stellar continuum fits to higher metallicities relative to the gas-phase metallicities. Accurate characterization of these H II regions requires additional inclusion of WR stars in the stellar population synthesis models. Our FUV spectra demonstrate that the $\sim 900-1200$ Å FUV can provide a strong test-bed for future WR atmosphere and evolution models.

Keywords: Chemical abundances (224), Wolf-Rayet stars (1806), Ultraviolet spectroscopy (2284), H II regions (694), Spiral galaxies (1560)

1. INTRODUCTION

The history of a galaxy can be traced from its cumulative abundance pattern, as abundances of heavy elements increase with time as successive generations of stars return their newly synthesized elements to the interstellar medium (ISM). Starforming regions (H II regions) are privileged sites to measure the chemical abundances in galaxies, near and far, due to

their ubiquitous strong emission lines in the rest-frame optical regime. While the majority of nebular studies come from optical observations, the far-ultraviolet (FUV; defined here as 1200 - 2000 Å) is a rich wavelength regime with many nebular diagnostic features that are complementary to those in the optical. Recently, the *James Webb Space Telescope (JWST)* has enabled rest-frame optical and ultraviolet (UV) spectra of intermediate and high redshift galaxies, ushering in a new era of chemical abundance studies across cosmic redshifts (e.g., Arellano-Córdova et al. 2022; Curti et al. 2023; Maseda et al. 2023; Nakajima et al. 2023; Rogers et al. 2023). Robust abundance measurements are key to deciphering the complex physical and evolutionary processes of galaxy formation and

^{*} Based on observations made with the NASA/ESA Hubble Space Telescope, obtained from the Data Archive at the Space Telescope Science Institute, which is operated by the Association of Universities for Research in Astronomy, Inc., under NASA contract NAS 5-26555.

growth. In this regard, securing details of present-day abundances in star forming regions, which better allow us to interpret the higher redshift spectra, is crucial for forming the basis of our understanding of the chemical evolution of the universe.

Different elements trace different portions of chemical evolution owing to the different times scales of their nucleosynthetic production. On short time scales (< 10 Myr), massive stars (> 10 M_{\odot}) forge heavier elements through the α -process which fuses α -particles into successfully more massive elements to create oxygen, neon, magnesium, silicon, and beyond up to iron. When these massive stars reach the iron-peak they explode as supernova and deposit these α -enriched elements into the ISM. Carbon and nitrogen, crucial elements for the formation of dust and regulation of ISM conditions, are not significantly produced by the α -process. Rather, the primary mechanism to produce nitrogen and carbon is thought to be neutron capture within asymptotic giant branch (AGB) stars, occuring on longer timescales. AGB stars are evolved lower mass (0.5–8 M_☉) stars with inert cores of carbon and oxygen. These AGB stars are thought to be the primary source of nitrogen at lowmetallicity (12+log(O/H) $\lesssim 8.0$; $Z \lesssim 0.2 Z_{\odot}$), with enrichment timescales (~ 250 Myr; Henry et al. 2000) that occur significantly after the most massive stars have exploded as supernovae.

At higher metallicity ($Z \gtrsim 0.2 Z_{\odot}$), the carbon-nitrogenoxygen (CNO) cycle provides a "secondary" source of N, meaning that it is metallicity-dependent. The CNO cycle uses trace amounts of carbon and oxygen as catalysts in a chain of reactions that convert H to He. Nitrogen is mostly produced in CN branch of the CNO cycle, which uses ¹²C as a reaction catalyst and creates ¹⁴N as a byproduct. The slowest "bottleneck" step of this branch is the $^{14}{\rm N}(p,\gamma){\rm O}^{15}$ step because it has a relatively low cross-section, allowing nitrogen to build up in the cores of high-metallicity massive stars. Convection can then dredge up nitrogen to the surface, where stellar winds can advect it into the ISM. This process can enhance N-production during certain phases of massive star evolution, such as the Wolf Rayet (WR) star phase, where stellar winds are especially strong. Measuring the relative chemical abundance (e.g. N/O or C/O) describes which of these processes a galaxy has undergoing and what the past star formation history of the galaxy looks like.

Recent observations of high-redshift galaxies have raised questions about the standard view of chemical abundances. For instance, deep rest-frame FUV observations of the galaxy GN-z11 find strong N IV] $\lambda 1486$, N III] $\lambda 1750$, and C III] $\lambda \lambda 1907,1909$ emission lines that suggest that the galaxy has been enriched to super solar nitrogen abundances just a few 100 Myr after the Big Bang (e.g., Maiolino et al. 2023; Charbonnel et al. 2023; Senchyna et al. 2023). This is far too

rapid for enrichment by AGB stars. Previous studies suggest that either WR, super massive stars, tidal disruption events, or active galactic nuclei environments could be responsible for the high nitrogen abundances (e.g., Matsuoka et al. 2017; Cameron et al. 2023; Kobayashi & Ferrara 2024). However, the nitrogen and carbon lines observed within GN-z11 are rarely detected in local star-forming galaxies, such that a complete understanding of the production and origin of these features has not fully been revealed. The origin of these features requires a multi-wavelength approach that incorporates both the stellar and nebular physics.

UV spectra offer a unique glimpse into the processes occurring in star-forming galactic environments. In particular, the FUV regime contains a rich diversity of features that can simultaneously characterize the ionizing sources, feedback energetics, and gas conditions within galaxies. FUV stellar spectra of ionized regions (H II) trace the massive star population, as they are dominated by P-Cygni stellar wind features, composed of a combination of broad, blueshifted absorption and redshifted emission. The so-called stellar wind P-Cygni profiles are produced by strong, radiativelydriven stellar photosphere winds (e.g., Castor et al. 1975; Lamers et al. 1999). Winds from O-stars are usually ionized to the N⁺³, C⁺⁴, and Si⁺⁴ ionization states (Lamers et al. 1999). However, none of these ionization states have strong resonant lines blueward of Ly α (note that N IV λ 1720 is a non-resonant line). The lines that are available, N V $\lambda\lambda$ 1238,1246, Si IV $\lambda\lambda$ 1393,1403, and C IV $\lambda\lambda$ 1548,1550, trace adjacent ionization stages. As such, these stellar wind signatures are highly sensitive to the temperature (and, therefore, the age), density, and metallicity of the winds of the most massive / luminous stars. This sensitive dependency on stellar properties has important ramifications for which lines trace which stars. For instance, the Si IV $\lambda\lambda$ 1392,1402 doublet traces lower ionized gas than the peak ionization, such that Si IV is typically only observed in populations with cooler stars, such as evolved Giants or B-stars. The N V $\lambda\lambda$ 1238,1242 doublet on the other hand traces more highly ionized gas and is only found in the hottest / youngest stellar populations.

In this paper we present HST/COS FUV spectral observations for 9 H II regions in M101 in § 2 and use these spectra to explore the stellar features and nebular emission. M101, also known as NGC 5457, is an invaluable target for investigating the stellar and nebular properties across spiral galaxies. Its utility stems from its proximity, allowing for detailed, spatially-resolved investigations, and its face-on orientation, which presents an unobstructed view of its spiral arms and associated nebulae, providing a comprehensive look at the distribution and composition of stellar and nebular properties. Our sample of H II regions and spectral observations are described in Sections 2 and 3, respectively. In Section 4,

we perform stellar continuum fits to determine the average properties of the massive star populations. We discuss the FUV spectral characteristics of this sample in Section 5, including the stellar continuum properties in § 5.1 and the presence of Wolf-Rayet features and He II emission in § 5.2, In § 5.5.2 we examine the nebular C and O emission features and C ionization correction factors (ICFs) from our grid of photoionization models in order to perform an exploratory FUV C/O abundance analysis and compare to optical C/O measurements. Our conclusions are given in Section 6.

2. THE M101 H II REGION SAMPLE

For the present study, we targeted the star-forming regions identified by Skillman et al. (2020) as very high surface brightness H II regions in M101. In particular, these H II regions contain detections of 4-5 intrinsically-faint auroral collisionally-excited lines (CELs; see Table 1) and the even fainter C II λ 4267 recombination line (RL) in their high-quality optical spectra from the CHemical Abundances Of Spirals (CHAOS; Berg et al. 2015) project study of M101 (Croxall et al. 2016). In total, Skillman et al. (2020) presented 10 H II regions. For this work, we targeted the same sample of 10 H II regions, but one of the UV spectral observations failed, resulting in a sample of 9 H II regions.

We note that Skillman et al. (2020) assumed the same properties for M 101 as in Croxall et al. (2016), i.e., a distance of 7.4 Mpc (Ferrarese et al. 2000), resulting in a spatial scale of 35.9 pc/arcsec; however, Beaton et al. (2019) have made a (hopefully) definitive determination of the distance to M101 of $6.52 \pm 0.12_{stat} \pm 0.15_{sys}$ Mpc, with a resulting scale of 31.6 pc/arcsec. We have adopted the updated Beaton et al. (2019) distance here, although updates to the distance to M101 will not affect the major conclusions of this paper. We have also assumed disk scalings of $R_{25} = 864''$ (radius of B_{25} mag arcsec⁻²; Kennicutt et al. 2011) and $R_e = 198''$ (half-light radius; Berg et al. 2020), an inclination angle of 18°, and a major-axis position angle of 39° (Walter et al. 2008).

CHAOS uses the Multi-Object Double Spectrographs (MODS, Pogge et al. 2010) on the Large Binocular Telescope (LBT, Hill et al. 2010) to observe moderate-resolution ($R \sim 2000$) optical spectra (3,200 Å $\lesssim \lambda \lesssim 10,000$ Å) of a large numbers of H II regions in spiral galaxies. As part of the CHAOS program, very high quality spectra of 74 H II regions in M101 (Croxall et al. 2016) were obtained that allowed direct determinations of absolute and relative abundances across a broad range of parameter space. As an extension of the CHAOS project, Skillman et al. (2020) examined the M101 spectra for the optical RL and found detections of the C II $\lambda 4267$ line in 10 H II regions.

Opt. CHAOS Apertures. FUV COS Apertures 10 45 11 3 2 68

Figure 1. Image of M101 showing the H II regions targeted by the CHAOS survey using slit masks (yellow lines; Croxall et al. 2016) and the 10 regions in which recombination-line C II λ 4267 emission was detected (green diamonds; Skillman et al. 2020). These 10 regions were followed-up with *HST/COS* observations as part of the HST-GO-15126 program (PI: Berg). The regions numbers correspond to those given in Table 1.

3.1. LBT/MODS Optical Spectra

The optical observations presented here were previously reported in Croxall et al. (2016) and updated in Berg et al. (2020), where the interested reader can find details of the observations and data reduction. Here we briefly summarize.

Optical spectra of M101 were taken using MODS1 on the LBT during the spring semester of 2015. We obtained simultaneous blue and red spectra using the G400L (400 lines mm⁻¹, R \approx 1850) and G670L (250 lines mm⁻¹, R \approx 2300) gratings, respectively. The primary objective of the CHAOS program is to detect the intrinsically weak temperaturesensitive auroral lines in the wavelength range from 3200-10,000 Å in order to determine direct abundances. Although not a design goal of the program, the observations of M101 were sensitive enough to detect RL emission from the C II λ 4267 line. Recombination line observations are typically made at higher spectral resolution than in the CHAOS program because O II RLs are tightly clustered. However, the $\lambda 4267$ line is well isolated, making C II RL detections and abundances of C⁺²/H⁺ possible from the MODS spectra. Further discussion of the $\lambda 4267$ RL detections can be found in Skillman et al. (2020).

The original footprint of CHAOS observations of M101 is shown in Figure 1, with the 10 regions from the current sample designated with green diamonds. The present H II

Table 1	Properties of	of M101	Н п Рес	rione from	the	CHAOS	Curveve
Table 1.	riopeines o	וטוועו וכ	ппке	210118 1110111	uie	CHAUS	Surveys

					A	uroral Lin	e Detecti	ons				
Region	Name	R.A., Decl.	Location ID	$\frac{R}{R_e}$	12+log(O/H)	[О ш]	[N II]	[S III]	[О п]	[S II]	Не п	WR
1	H1013	14:03:31.3,+54:21:05.81	+164.6+009.9	0.89	8.60 ± 0.03	√	√	✓	√	√		_
2	H1052	14:03:34.1,+54:18:39.60	+189.2-136.3	1.30	8.58 ± 0.02	✓	✓	✓	✓	√		1
4	NGC 5462	14:03:53.0,+54:22:06.80	+354.1+071.2	1.89	8.51 ± 0.10	✓	✓	✓	✓	✓		
5	NGC 5462	14:03:53.8,+54:22:10.81	+360.9+075.3	1.99	8.51 ± 0.02	✓		✓	✓	✓		
6	NGC 5447	14:02:30.5,+54:16:09.89	-368.3-285.6	2.42	8.45 ± 0.02	✓	✓	✓	√	√		/
7	NGC 5455	14:03:01.1,+54:14:27.97	-099.6-388.0	2.19	8.39 ± 0.01	✓	✓	✓	√	√		/
8	NGC 5447	14:02:27.8,+54:16:25.14	-392.0-270.1	2.49	8.36 ± 0.02	✓	✓	✓	√	√		/
9	H1216	14:04:10.9,+54:25:19.20	+509.5+264.1	3.56	8.29 ± 0.06	√	✓	✓	✓	✓	✓	
10	NGC 5471	14:04:29.0,+54:23:48.56	+667.9+174.1	3.81	8.16 ± 0.02	√	✓	✓	✓	✓	/	

NOTE— Properties of the 9 H II regions from the M101 sample that were observed with HST/COS. Note that 10 regions were originally proposed, but the HST/COS observations of Region 3 failed. Column 1 lists the region numbers that we adopt in this paper, whereas Column 2 gives the regions common name from either the New General Catalogue (NGC) or the Hodge et al. (1990) catalogue. Column 3 gives the right ascension (R.A.) and declination (Decl.) in J2000 and Column 4 gives the CHAOS ID from Croxall et al. (2016), which is composed of the offset R.A. and Decl., in arcseconds, from the galaxy content. Column 5 lists the galactocentric distance as a fraction of the effective radii, R_e , and Column 6 lists the oxygen abundances, as updated by Berg et al. (2020). Columns 7–11 highlight regions with significant auroral line detections of $[O III] \lambda 4363$, $[N II] \lambda 5755$, $[S III] \lambda 6312$, $[O II] \lambda \lambda 27230$,7330, and $[S II] \lambda \lambda 4069$,4076. We note in columns 12 and 13 which H II regions have detections of narrow, nebular He II $\lambda 4686$ emission and broad Wolf-Rayet features.

region sample has a radial coverage of $0.2 \lesssim R/R_{25} \lesssim 0.8$ and spans a range of 0.44 dex in oxygen abundance. Properties determined for the H II regions in the present sample by the CHAOS survey are reported in Croxall et al. (2016); a subset of important properties are listed in Table 1.

3.2. HST/COS UV Spectra

In order to measure the UV stellar and nebular properties of the H II regions in M101 we obtained Cycle 25 *HST*/COS observations (program HST-GO-15126, PI: D. Berg). Berg et al. (2016) demonstrated the utility of simultaneously observing the O III] $\lambda\lambda$ 1661,1666 and C III] $\lambda\lambda$ 1907,1909 nebular emission lines in the FUV afforded by the large wavelength coverage (1282–2148 Å in Segment A) of the low-resolution G140L grating. Adopting this observing strategy, we observed each of 9¹ H II regions in M101 for 1-3 orbits.

Due to the proximity of M101, the large H II regions fill the COS aperture; however, target image acquisition was efficiently achieved using a pointing offset from a nearby bright star. We used deep B-band LBT Large Bincoluar Cameras (LBCs) imaging from the OSU Monitor program (e.g., Neustadt et al. 2021) to select bright, isolated stars near our target H II regions. The excellent astrometry of these images provided precise positions of the offset stars and allowed us to accurately determine offsets. We used the ACQ/IMAGE mode with the PSA aperture and MirrorB (due to the brightness of the offset stars) with the COS/NUV configuration to

acquire the stars and then blind offset to the target H II regions.

COS FUV spectral observations were taken in the TIME-TAG mode using the 2.5" PSA aperture and the G140L grating at a central wavelength of 1280Å. We used the FP-POS = ALL setting, which takes four images offset from one another in the dispersion direction, increasing the cumulative S/N and mitigating the effects of fixed pattern noise. The four positions allow a flat to be created and for the spectrum to fall on different areas of the detector to minimize the effects of small scale fixed pattern noise. Spectra from the 9 successful observing visits were processed with CALCOS version 3.3.4. In order to gain signal-to-noise, we followed Berg et al. (2019b) and re-binned the spectra by a factor of six in the dispersion direction and smoothed with a 3-pixel boxcar kernel. Nominally, the COS has a resolution of $R \sim 2000$ for point sources, but this resolution is degraded for nebulous regions that fill the aperture. By measuring individual photosphere absorption lines in our spectra, we found a typical FWHM $\sim 300 \text{ km s}^{-1}$, which corresponds to $R \sim 1000$.

Figure 2 shows the FUV spectra for the 9 H II regions observed. The observed wavelength coverage of G140L is $\sim 900-1195$ for Segment B and $\sim 1282-2000$ for Segment A². The 105 Å gap between Segments A and B mitigates the risk of strong Geocoronal Ly α emission on the detector, however, this also causes our spectra to miss the N V $\lambda\lambda$ 1238,1242 stellar wind feature. The spectra were corrected for the redshift of M101 (z=0.0008), but not for the

¹ All 10 H II regions in the Skillman et al. (2020) sample were proposed for in program HST-GO-15126, however, the target acquisition failed on the final target (region 3, NGC 5461). Since Space Telescope Science Institute deems a program as successful when 90% complete, the observation was not repeated.

 $^{^2}$ Segment A coverage is quoted out to 2148 Å, however, previous experience with G140L spectra suggest G140L Segment A spectra only have utility out to ~ 2000 Å.

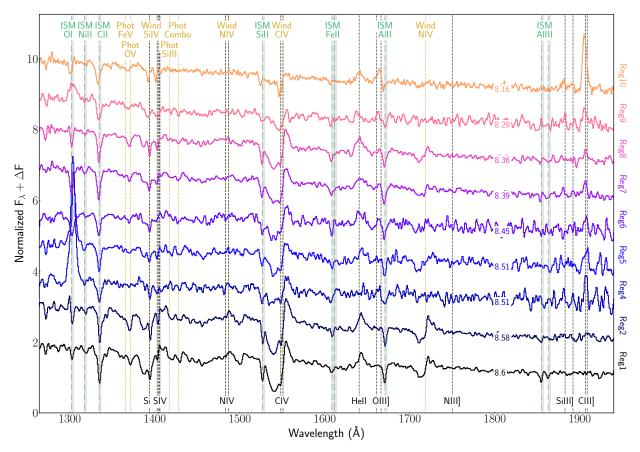


Figure 2. HST/COS G140L spectra of the 9 H II regions in the CHAOS M101 sample, normalized at $\lambda1800$ and ordered by increasing gas-phase oxygen abundance from top to bottom. The location of potential UV spectral features are denoted for ISM absorption lines (green long-dashed lines), stellar wind and photospheric features (gold dashed lines), and nebular emission lines (black dashed lines). The combination of photospheric lines at ~ 1430 Å contains C III $\lambda\lambda1426,1428$ and Fe V $\lambda\lambda1429,1430$ in O stars (e.g., de Mello et al. 2000). Note that the resonant transitions that produce stellar wind P-Cygni profiles can also have ISM absorption components. Due to the low-resolution of the G140L spectrum, MW features (locations indicated by gray bands) are not resolved and may contaminate other features. Note that there is also Geocoronal O I emission near $\lambda1300$ in the spectra of Regions 4 and 5.

Table 2. Comparison of Stellar and Gas Properties

					Gas Pro	operties					
Reg. #	WR	E(B-V) _{SB99} (mag.)	E(B-V) _{BPASS} (mag.)	Age _{SB99} (Myr)	Age _{BPASS} (Myr)	$Z_{\star,SB99} \ (Z_{\odot})$	$Z_{\star,BPASS} \ (Z_{\odot})$	O/H _{neb.} (O/H _☉)	N/O _{neb.} (N/O _⊙)	ΔZ_{SB99} (Z_{\odot})	$\begin{array}{c} \Delta Z_{BPASS} \\ (Z_{\odot}) \end{array}$
1	√	0.218 ± 0.003	0.178 ± 0.004	1.94 ± 0.03	3.65 ± 0.56	1.00 ± 0.03	0.88 ± 0.01	0.81 ± 0.01	0.81 ± 0.01	0.19	0.06
2	✓	0.197 ± 0.004	0.172 ± 0.003	1.60 ± 0.04	2.76 ± 0.19	1.00 ± 0.03	0.88 ± 0.01	0.78 ± 0.01	0.74 ± 0.01	0.22	0.10
4		0.239 ± 0.035	0.258 ± 0.020	4.12 ± 2.33	4.15 ± 2.38	0.49 ± 0.13	0.51 ± 0.07	0.66 ± 0.02	0.44 ± 0.04	-0.17	-0.15
5		0.245 ± 0.014	0.251 ± 0.015	2.42 ± 0.64	5.57 ± 4.03	0.89 ± 0.11	0.47 ± 0.04	0.66 ± 0.01	0.43 ± 0.01	0.23	-0.19
6	✓	0.311 ± 0.021	0.311 ± 0.016	1.64 ± 0.77	1.83 ± 2.06	0.93 ± 0.15	0.60 ± 0.03	0.58 ± 0.01	0.55 ± 0.01	0.35	-0.03
7	✓	0.195 ± 0.005	0.182 ± 0.005	2.42 ± 0.11	4.30 ± 1.00	0.78 ± 0.05	0.52 ± 0.02	0.50 ± 0.01	0.55 ± 0.01	0.28	0.02
8	\checkmark	0.174 ± 0.005	0.159 ± 0.005	2.26 ± 0.09	2.40 ± 0.96	0.99 ± 0.04	0.55 ± 0.02	0.47 ± 0.01	0.59 ± 0.01	0.52	0.08
9		0.169 ± 0.011	0.192 ± 0.011	3.31 ± 2.16	7.14 ± 3.40	0.62 ± 0.15	0.28 ± 0.07	0.40 ± 0.01	0.33 ± 0.03	0.22	-0.12
10		0.158 ± 0.016	0.150 ± 0.007	9.69 ± 3.90	12.2 ± 3.05	0.29 ± 0.06	0.22 ± 0.02	0.30 ± 0.01	0.34 ± 0.01	-0.01	-0.08

NOTE—Stellar and nebular properties for the nine H $_{\rm II}$ regions studied here. The stellar properties are derived from the luminosity-weighted stellar continuum fits described in Section 4, where columns 3–8 correspond to the derived reddening, age, and metallicity of the massive star population from both SB99 and BPASS fits. The differences between the stellar model metallicities and the gas-phase metallicity are listed in columns 9–10. For comparison, regions with identified WR features are noted in Column 2, while the nebular O/H and N/O abundances are given in columns 9–10. All abundances are relative to the solar scale from Asplund et al. (2021), e.g., N/O_{neb.} = 0.813 N/O_{\odot} is equivalent to 81.3% the solar N/O value.

small offsets resulting from the galactocentric rotational velocity of a given H II region.

In order to allow a close comparison of feature trends, the spectra in Figure 2 are vertically offset from one another and ordered from top to bottom by increasing metallicity. Nebular features are labeled by gray short-dashed lines, while stellar wind and photospheric features are gold, and ISM absorption is labeled green. Some features are complex combinations of multiple components, such as C IV, which can have stellar, nebular, ISM components, and, at the small redshift of M101, contamination from Milky Way absorption. Some features are clearly sensitive to metallicity, such as the S IV, C IV, and N IV stellar wind features, which strengthen with increasing metallicity, and the C III] nebular emission, which generally weakens in strength at higher metallicity. We also note the presence of He II emission, which can be both stellar and nebular in origin. As we will see later, the strong, broad He II features in regions 1, 2, 6, 7, and 8 are likely stellar, as strong Wolf-Rayet (WR) features are noted in their optical spectra. On the other hand, narrow He II emission was found in the optical spectra of regions 9 and 10, so their UV He II features may be nebular (see Table 1).

4. STELLAR CONTINUUM FITTING

The interplay between gas and stars is one of the most fundamental, yet unsettled, drivers of galactic baryon evolution. The FUV ($\sim 912-2000 \text{ Å}$) is arguably the richest spectral regime in diagnostic features characterizing the processes involved in the baryon feedback cycle. This spectral range not only provides access to the only strong C nebular emission lines, but also reveals stellar wind and photospheric features that are more sensitive to the age and metallicity of the ionizing stellar population than any optical diagnostic features (e.g., Chisholm et al. 2019). Consequently, the FUV continuum offers a valuable means to characterize the stellar clusters within H II regions, enabling a direct link between the properties of massive stars and the nebular emission lines they power. Further, in the high surface-brightness H II regions targeted here, the ionizing stellar population recently formed from the surrounding gas such that the nebular and stellar chemical compositions are expected to be similar. Here we take advantage of the HST/COS FUV spectra of M101 to model the stellar continua of our H II region sample and better understand the conditions powering their observed emission-line spectra.

4.1. Fitting Method

We fit the stellar continuum following the procedure detailed in Chisholm et al. (2019). This method uses stellar population synthesis modeling to characterize the ages and metallicities of the ionizing stellar populations. Fitting was performed as a linear combination of single-age, fully theo-

retical stellar continuum burst models matched to the nonionizing FUV continua of our sample. We use two sets of theoretical stellar models: (1) single star models from Starburst99 (SB99; Leitherer et al. 1999) and (2) binary star models from BPASS v2.2.1 (Eldridge et al. 2017; Stanway & Eldridge 2018). With both set of models we employ a range of possible metallicities covering 0.05, 0.20, 0.40, 1.0, and $2.0~\rm Z_{\odot}$ and a range of burst ages (1–40 Myr), use a highmass cutoff of $100~M_{\odot}$. The best intrinsic spectrum is combined with a foreground dust screen model and the Reddy et al. (2016) attenuation law to determine the reddening due to dust (E(B-V)).

We fit the entire observable range of the HST/COS G140L segment A spectra, covering $\sim 1300-2000$ Å. Next, we convolved the 0.4 Å resolution of the SB99 models and the 1 Å resolution of the BPASS models to the spectral resolution of the individual H II region spectra (e.g., Meynet et al. 1994; Leitherer et al. 1999). In order to isolate the purely-stellar portions of the spectra, we mask any features that are not produced by the stars, including Milky Way absorption features and ISM emission and absorption lines from the H II regions. A list of features considered for masking can be found in Leitherer et al. (2011). The errors on the stellar fits were determined using a boot-strap Monte Carlo procedure, where 300 iterations were performed (the number of iterations needed to reach convergence for spectra with these S/N ratios; Chisholm et al. 2019) using a modified version of the observed spectrum with error randomly sampled from a normal distribution. Further details of the fitting method can be found in Chisholm et al. (2019).

The stellar continuum modeling simultaneously constrains the light-weighted age, metallicity, and reddening (E(B-V)) of the ionizing massive star population, the results of which are listed in Table 2. We note that Regions 1 and 2 were best fit by SB99 with super-solar light-weighted metallicities that are significantly higher than their gas-phase abundances. Therefore, we reran the SB99 fits without the $2.0~\rm Z_{\odot}$ model, effectively enforcing an upper metallicity limit of solar for these two H II regions in order to more closely match the observed gas-phase oxygen abundance range.

The uncertainties reported from the Monte Carlo procedure for the reddening, age, and metallicity of the stellar population are listed in Table 2. In general, the uncertainties on the reddening and metallicity values are small ($\lesssim 25\%$ for SB99 and $\lesssim 10\%$ for BPASS). However, a few of the regions have large age uncertainties, especially the regions lacking WR features and regions older than 5 Myr. These more uncertain ages are likely due to degeneracies arising from the lack of strong spectral features able to distinguish older population ages. Similarly, Sirressi et al. (2022) used integrated stellar population spectra with the same continuum-fitting method presented here and compared to resolved star pho-

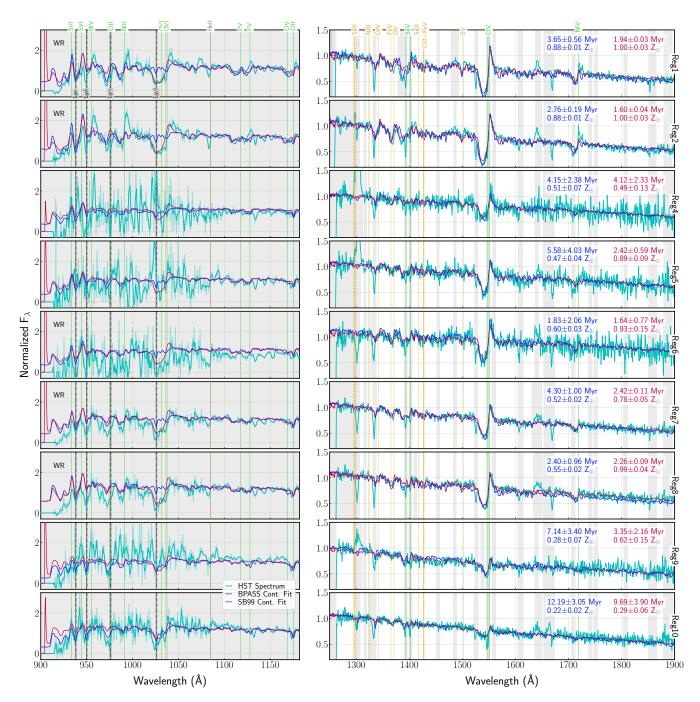


Figure 3. Luminosity-weighted best fit stellar models to the *HST/COS* FUV spectra of the M101 H II region sample. Observed spectra are shown in turquoise, with the best-fit stellar Starburst99 and BPASS models overlaid in red and blue, respectively. Rest-wavelengths of stellar wind and photospheric features are shown by solid green and dashed gold lines, respectively. Additionally, H and He lines are denoted by solid gray lines; the MW H lines are indicated with dashed-dotted gray lines. Fits were performed after masking any contamination from MW sky lines, ISM absorption features, and nebular emission lines (gray-shaded bands). The resulting age and metallicity that best characterizes the ionizing stellar population is labeled in the upper right hand corner of each panel for both the Starburst99 (red) and BPASS (blue) models. We also highlight the excellent PowR WR model fit to the N III λ991 feature of Region 1 in the yellow inset box. In general, there is a progression from strong stellar features at the highest metallicities (top) to small features at the lowest metallicities (bottom).

8 BERG ET AL.

tometry to show that ages could be measured with high accuracy (< 1 Myr) for populations with ages between 2 and 5 Myr. This suggests that our youngest stellar ages may have underestimated uncertainties, but they are robust within 1 Myr.

4.2. SB99 and BPASS Comparison

The best stellar continuum fits using both SB99 and BPASS are shown in Figure 3, over-plotted on the observed *HST* spectra, where the masked portions for each H II region are denoted by gray bands. However, the SB99 and BPASS stellar continuum fits look very visually similar for most of the H II regions over the fit range (right column panels). Comparing the results in Table 2, we find that the BPASS fits have older light-weighted ages than the SB99 models by 1.6 Myr on average. Countering this effect, on average, the BPASS fits have 23% lower metallicities than the SB99 fits. The fitted reddening values are similar between SB99 and BPASS, with an average difference of only 0.006.

A visual comparison of the stellar features in the SB99 and BPASS models relative to the observed spectra can provide further insight. In the fitted part of the spectra (right column panels), there are three stellar wind features – Si IV $\lambda\lambda 1393,1403,$ C IV $\lambda\lambda 1548,1550,$ and N IV $\lambda 1720$ – whose wind profiles are all fit reasonably well by both SB99 and BPASS. However, excess Si IV and N IV emission are seen in several of the WR regions. Additionally, neither SB99 nor BPASS have WR prescriptions that can produce sufficiently broad He II emission in these regions.

While not fit with the stellar models, we also examined the bluest portion of the COS spectra. The $\sim 900-1200~\textrm{Å}$ portion of the FUV is notoriously difficult to fit due to the densely packed suite of stellar and ISM lines in the observed galaxy and low-ionization resonance lines formed in the intervening gas, including numerous Lyman series H lines and Lyman and Werner bands of H_2 (e.g., Tumlinson et al. 2002). This leaves little to no uncontaminated continuum to fit (see, e.g., Willis et al. 2004). Therefore, it is interesting that both the SB99 and BPASS models produce good overall fits to the observed spectra, despite being unconstrained by the data in this challenging wavelength regime.

On the other hand, the fit of the SB99 models to the most prominent features in the bluest spectral regime is rather impressive. In particular, the SB99 models trace and confirm the O VI $\lambda\lambda$ 1032,1038 P-Cygni profile in Regions 1, 2, 5, 6, 7, and 8. The O VI feature is further evidence of very young stars in these regions (< 3 Myr; see next section), favoring the younger ages of the SB99 fits. Note, however, that the BPASS models do not incorporate X-ray winds, and so they will not be able to fit the O VI (I.P. \gtrsim 114 eV) feature. It would also be useful to fit the age-sensitive N V $\lambda\lambda$ 1238,1242 feature in order to confirm the young ages of the massive star

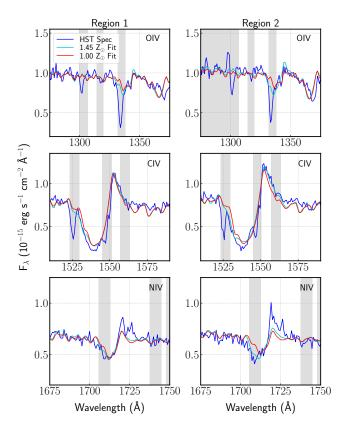


Figure 4. Comparison of the O IV, C IV, and N IV stellar features in Regions 1 and 2 for Starburst models with different light-weighted metallicities. Regions masked for possible contamination from MW sky lines or ISM absorption features are indicated by gray-shaded bands. There is very little difference between the two sets of models, and the models fail to reproduce the peak of the emission in the N IV P-cygni profile, demonstrating the need for both improved models and higher resolution and S/N spectra.

population, but N V unfortunately falls in the G140L gap (implemented to avoid Geocoronal Ly α) at the low redshift of M101.

4.3. Single- and Mutli-Population Comparison

Typically, simple stellar populations (SSPs) assuming a single-burst (single-population) are used to characterize the stellar continuum of an H II region, while multiple single-burst models (multi-population) are combined to characterize the integrated spectra of galaxies. As demonstrated for Region 10 (NGC 5471) in Figure 5, many of the H II regions in M101 are giant complexes containing multiple knots of star-formation and earning them their own NGC classifications. For example, García-Benito et al. (2011) performed a photometric study of the star formation history of NGC 5471 showing that star formation has been more or less continuous for at least 100 Myr. Further, they found that both the integrated photometry and resolved-star color-magnitude di-

agram of NGC 5471 is consistent with star formation of two different ages.

More recently, Sirressi et al. (2022) used Legacy ExtraGalactic UV Survey (LEGUS) HST multiband photometry and CLusters in the UV as EngineS (CLUES) FUV HST/COS spectroscopy of 20 young stellar clusters hosted in 11 nearby star-forming galaxies to examine their stellar populations. Using single-population fits, two-population fits, and the same multi-population fit method used here, Sirressi et al. (2022) found that most of the star-forming regions examined (16/20) are populated by two or more stellar populations. In fact, a second population was required for these regions to accurately reproduce the observed level of spectral continuum and the P-Cygni line profiles simultaneously. Given the complicated nature of the giant H II regions in M101 and their complex star formation histories, we adopted the multi-population method to characterize their stellar continua in our analysis above.

To test the validity of our multi-population assumption, we also fit the two regions showing the strongest stellar features (Regions 1 and 2) with single-population fits. The resulting single-population SB99 and BPASS fits (dashed-lines) are shown in Figure 6 in comparison to their corresponding multi-population fits (solid lines). In general, the multi-population fits better fit the stellar wind profiles. For Region 1, the single- and multi-population SB99 fits show little difference, but the multi-population BPASS fit more closely matches the Si IV $\lambda\lambda$ 1393,1403 and C IV $\lambda\lambda$ 1548,1500 outflow profiles than the single-component BPASS fit. For Region 2, both the SB99 and BPASS fits show differences between the single- and multi-population fits. In particular, the multi-population fits better reproduce the Si IV $\lambda\lambda$ 1393,1403, C IV $\lambda\lambda$ 1548,1500, and the N IV λ 1720 profiles.

The resulting stellar continuum properties for the single-and multi-population SB99 and BPASS fits are compared in Table 3. In general, the reduced χ^2 values are similar between the single- and multi-component fits, but are smaller for the multi-component fits. Additionally, the multi-component fit properties have much smaller uncertainties relative to the single-component fits. However, an important aspect of the multi-population BPASS fits is that they allow for slightly older ages. We, therefore, conclude that there are not significant differences between the single-population and multi-population fits, but that the multi-population fits provide a small improvement in the complex H II regions of M101.

5. CHARACTERISTICS OF THE FUV SPECTRA OF M101

5.1. Stellar Continuum Properties

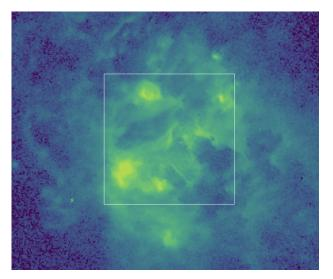


Figure 5. This image of Region 10 (NGC 5471) using the F656N filter on HST/WFPC2 (PID: HST-GO-6829; PI: You-Hua Chu) shows multiple knots of H α emission composing the complex, giant H II region. This suggests that multiple star associations are contributing to the gas ionization. For reference, the white box spans $10'' \times 10''$.

Figure 3 shows stellar-wind P-Cygni profiles of O VI $\lambda\lambda 1032,1038$, Si IV $\lambda\lambda 1393,1402$, C IV $\lambda\lambda 1548,1550$, and N IV $\lambda 1720$. Since more massive and luminous stars have shorter main sequence lifetimes, the P-Cygni profile strengths constrain the age of the ionizing stellar population. Higher ionization state profiles, such as O VI and N V, are strongest in stars with lifetimes of 2–3 Myr, while lower ionization state profiles, such as C IV and Si IV, are more prominent in stars with lifetimes near 5 Myr. This trend can be seen in Figure 3, were the C IV profile is generally stronger for the lowest stellar population ages and weak for the highest ages. This is further evidenced by Regions 1, 2, 6, and 7 having the strongest O VI P-Cygni profiles and the youngest SB99 ages. Note, however, the O VI wind profile is contaminated by strong Ly β absorption or emission, and so requires careful evaluation.

P-Cygni stellar-wind profiles are also sensitive to the metallicity of the stellar photospheres, where continuum photons are absorbed and drive gas from the stellar surface. However, this metallicity sensitivity declines above solar. In Figure 4, we show the O IV, C IV, and N IV stellar features for H II regions 1 and 2 in our sample, both of which were initially best fit with a super-solar luminosity-weighted stellar continuum metallicity. In comparison, we show their respective adopted best-fit $Z = Z_{\odot}$ stellar continuum models (red) and a super-solar $Z = 1.45 Z_{\odot}$ model (cyan). In both regions, the O IV λ 1341 photospheric feature is well fit by both models blueward of the deep C II λ 1335 ISM absorption feature. The C IV $\lambda\lambda$ 1548,1550 wind profiles are also well fit, but the

14.63

9.72

Reduced χ^2_{SB99}

Reduced χ^2_{BPASS}

		Reg 1			Reg 2				
Property	Single Pop.	Multi. Pop.	Δ	Sing Pop		Multi. Pop.	Δ		
$Z_{\star,SB99}$ (Z_{\odot})	1.000 ± 0.238	1.000 ± 0.028	+0.000	1.000 ±	0.238	1.000 ± 0.030	+0.000		
$Z_{\star,BPASS}$ (Z_{\odot})	1.000 ± 0.238	0.876 ± 0.009	-0.124	$1.000 \pm$	0.238	0.881 ± 0.006	-0.119		
Age _{SB99} (Myr)	2.000 ± 2.000	1.940 ± 0.033	-0.060	$1.000 \pm$	2.000	1.600 ± 0.040	+0.600		
Age _{BPASS} (Myr)	1.000 ± 2.000	3.650 ± 0.558	+2.650	$1.000 \pm$	4.000	2.758 ± 0.192	+1.758		
$E(B-V)_{SB99}$ (mag.)	0.247 ± 0.033	0.218 ± 0.003	-0.029	$0.208 \pm$	0.028	0.197 ± 0.004	-0.011		
E(B-V) _{BPASS} (mag.)	0.223 ± 0.021	0.178 ± 0.004	-0.045	$0.180 \pm$	0.010	0.172 ± 0.004	-0.008		

Table 3. Comparison of Single- vs. Multi-Population Stellar Continuum Properties

NOTE— Comparison of the properties derived for the single- and multi-population SB99 and BPASS stellar continuum fits for Regions 1 and 2. The single-population fits tend to drive metallicities higher and ages lower relative to the multi-population fits. The multi-population fits also tend to have smaller reduced χ^2 values.

-0.41

-1.45

8.92

5.86

8.89

5.73

-0.03

-0.13

14.22

8.27

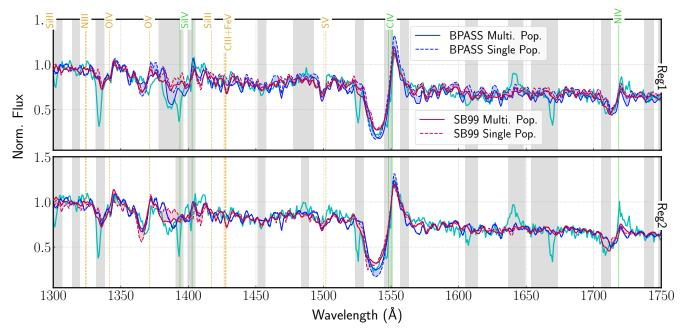


Figure 6. Comparison of the single-population best-fit stellar models (dashed lines) to the luminosity-weighted multi-population best-fit stellar models for Region 1 (top panel) and Region 2 (bottom panel). Observed spectra are shown in turquoise, with the best-fit stellar continuum models of Starburst99 (red) and BPASS (blue) overlaid. Differences between the single- and multi-population fits are emphasized by red and blue shading for the Starburst99 and BPASS models, respectively. (blue) models. As in Figure 3, stellar wind (solid green lines), photospheric features (dashed gold lines), and masked regions (gray-shaded bands) are shown. Overall, the multi-population fits better reproduce the observed stellar wind features, and are adopted for the analysis in this work.

models slightly underfit the depth and height of the P-Cygni profiles, regardless of metallicity. For the N IV $\lambda 1719$ wind feature, the absorption component of the P-Cygni profile is well fit blueward of the Ni II ISM absorption feature, but both models fail to reach the strength of the emission component. However, an additional N IV source may be contributing to this profile, as both Regions 1 and 2 appear to have N IV] $\lambda 1487$ emission in Figure 2.

In Figure 7, we compare the derived stellar population metallicity versus the nebular metallicity, as derived from the collisionally-excited lines direct method. As expected, the stellar and nebular metallicities generally correlate. Interestingly, the BPASS stellar metallicities are generally consistent with the nebular metallicities, while the SB99 stellar metallicities are offset to higher values, especially for the youngest-aged stellar populations. We fit a linear relationship to both the BPASS and SB99 trends using the Python Bayesian linear regression code linmix³, which is an implementation of the linear mixture model algorithm developed by Kelly (2007) to fit data with uncertainties on two variables, including explicit treatment of intrinsic scatter. The SB99 fit, shown in orange, indicates that, on average, the stellar metallicities are offset to higher metallicities by 0.25 dex. Figure 7 also shows a cluster of SB99 outliers at the highest stellar metallicities considered.

Taken as a whole, to match the strong stellar wind profiles of the youngest stellar populations that contain observed WR profiles (red diamonds in Figure 7), SB99 models require very young populations (< 3 Myr) that are more metalenriched than implied by their gas-phase metallicities. This may be because the lower-metallicity stellar evolution tracks do not produce significant amounts of evolved stars (Leitherer et al. 2011). Therefore, the code requires younger and more metal-enriched stellar populations to match the strong profiles in the populations with observed WR stars. Meanwhile, BPASS fits do produce sufficiently strong wind profiles that mimic the observed profiles at metallicities that are consistent with the observed gas-phase metallicities. This may be because the binary synthesis in BPASS allows for additional physical pathways to create the evolved (WR) stars observed in the spectrum (Eldridge et al. 2017). While BPASS does fit some of these lines better, many of the WR features are still poorly fit by population synthesis models. Thus, these stellar populations provide a strong test-bed to constrain future WR atmosphere and evolution models, and their incorporation to stellar population models.

5.2. He II Emission

Emission from He⁺² recombination produces the He II emission features commonly observed at $\lambda 1640$ in the rest-

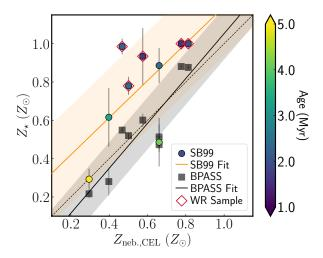


Figure 7. Comparison of the derived stellar population metallicity versus the nebular metallicity, as derived from the CEL direct method. As expected, the stellar and nebular metallicities generally increase in lock step, however, stellar metallicities are offset to higher values than nebular metallicities for the youngest-aged ionizing stellar populations. These outliers also tend to show WR features in their optical spectra (red diamonds), suggesting the WR phase is strongest for young (t < 3 Myr), metal-rich ($Z > 0.9Z_{\odot}$) massive stars.

frame FUV and $\lambda 4686$ in the rest-frame optical. He II emission is expected from a number of sources, including shocks, X-ray binaries, extremely metal-poor massive stars, and the winds of massive stars, such as WR stars. WR stars are an interesting source because they are extremely hot stars that have main-sequence lifetimes $\lesssim 5$ Myr (e.g., Abbott & Conti 1987; Crowther 2007) being observed during a short-lived supergiant phase. During this phase, WR stars produce broad He II emission lines in both the optical and FUV due to their strong winds that increase at higher metallicity (e.g., Schaerer & Vacca 1998).

Chisholm et al. (2019) used light-weighted stellar populations to show that the He II profile is also very sensitive to age. For the youngest populations in their study ($\lesssim 5$ Myr), He II λ 1640 has a strong, broad profile, while the oldest populations (> 20 Myr) show a weak He II absorption feature. They also found that their multiple-age fits to the FUV He II λ 1640 region were poor, especially in the presence of strong WR emission, with SB99 performing worse than BPASS. Similar to the results of Chisholm et al. (2019), Figure 3 shows that our best-fit stellar models fail to produce the requisite number of He II photons from WR stars to match the broad He II emission observed in our HST/COS spectra of H II regions in M101, especially for the youngest stellar populations (see, also, Leitherer et al. 2018). Further, Martins et al. (2023) used BPASS models with an initial mass function upper mass cutoff of 300 M_{\odot} to show that not even the

³ https://github.com/jmeyers314/linmix

winds of very-massive stars could reproduce the broad strong He II observed here.

5.3. Wolf-Rayet & Very Massive Star Features 5.3.1. Optical Characteristics

Given the low spectral resolution of the FUV spectra (300 km s⁻¹), the broad He II emission at λ 1640 is difficult to interpret. Therefore, it is useful to look to the optical spectra $(\Delta v \sim 150 \text{ km s}^{-1})$ to determine whether the He II emission appears narrow and nebular in origin or is broad due to WR or very-massive star (> 100 M_{\odot} ; VMS) winds. In Figure 8, we plot the He II portion of the FUV spectra in comparison to the two optical regions that are commonly used to spectroscopically identify the presence of WR stars. The first optical feature, known as the blue bump (middle column), is a complex of features near $\lambda 4650$, including N V $\lambda 4603$, N III $\lambda\lambda$ 4634,4641, C III λ 4647,4666, C IV λ 4658, and He II $\lambda 4686$. The second feature is a blend of C IV transitions at $\lambda\lambda$ 5801,5812, known as the red bump (right column). The shapes of these optical bumps help divide WR stars into three main classes (see Crowther 2007, and references therein): (1) WN stars: have H absorption lines and strong He and N emissions lines, especially in the blue bump, but can also have a few C lines; (2) WC stars: have strong He, O, and C emission lines, especially the C IV lines characteristic of the red bump, but lack N lines; and (3) WO stars: have strong lines from He and high-ionization lines from C and O.

Using the FUV and optical spectra presented here, we can characterize the WR nature of the stellar populations in our sample. We see that Regions 1 and 2 have clear N II $\lambda 4621$ and N III $\lambda\lambda 4634,4641$ emission in their blue bumps, along with weak detections of the N IV $\lambda 4057$ feature. Weak N features may also be present in Regions 6, 7, and 8. We also look for features indicative of WC stars. Just redward of the N emission in the blue bump (and blueward of [Fe III]), a second less prominent emission feature is seen in Regions 1 and 2, but it is difficult to determine whether this is due to C III or O II emission, or both. Further, the red C IV bump doesn't appear strongly in any of the H II regions in our sample, suggesting little to no contributions from WC stars in our spectra. Therefore, in the five regions with strong or weak optical WR features, we only significantly detect the blue WR bump, suggesting that WN stars are likely present. Using the Smith et al. (1996) N V λ 4057/N III 4603-4641 classification scheme, we find these stars are most consistent with late WN6-WN8 stars in Regions 1 and 2.

On the other hand, Martins et al. (2023) recently examined optical spectra of six of the H II regions presented here for signatures of VMS or WR features, but did find contributions from WC stars. However, Martins et al. (2023) used optical spectra from the SDSS and from GTC/OSIRIS from Esteban et al. (2020), which have slightly different aperture pointings,

sizes, and position angles than our CHAOS optical spectra. Because these H II regions have experienced intense star formation, they may contain a mixture of massive star types that are spatially distributed and so not equally captured in the different apertures used. In the present study, we took special care to design our HST/COS UV observations to have the same precise coordinates as the CHAOS optical spectra by employing target offsets from nearby point-sources. Therefore, the CHAOS optical spectra represent the closest spatial map to the FUV HST/COS spectra. However, there may still be differences in the stellar light captured between the FUV and optical spectra owing to the different aperture shapes and the vignetting of the COS aperture. These differences in observational setup may also be the source of discrepancies in identifying WR and VMS features. For example, Esteban et al. (2020, and, subsequently, Martins et al. (2023)) observe both the blue and red WR features in Region 7 (NGC 5455) and suggest that both WN and WC stars are present, while our spectra show no definitive signatures of WC stars.

5.3.2. FUV Characteristics

In agreement with past studies, the prominent WR emission in the M101 optical spectra corresponds to FUV spectra of young, metal-rich stellar populations (see Table 2). Interestingly, the M101 observations presented here suggest a threshold for strong WR emission of stellar $Z \gtrsim 0.78~Z_\odot$ ($Z \gtrsim 0.54~Z_\odot$) and $t \lesssim 3$ Myrs ($t \lesssim 5$ Myrs) for the SB99 (BPASS) models; slightly younger and less metal-rich than previously thought (e.g., Groh et al. 2014). This is shown in Figure 9 where we compare the stellar metallicities and ages of the full H II region sample to that of the WR subsample. H II regions with WR features only occupy the upper left young-age, high-metallicity regime of the plot.

Such young ages for WR stars, as indicated by the SB99 models, are somewhat surprising given that the main sequence H-core burning phase of massive stars that precedes the WR phase typically lasts longer than 3 Myr (e.g., 3.5 Mr for a non-rotating 60 M_☉ star Ekström et al. 2012). However, the situation is further complicated by the fact that massive star and WR evolutionary tracks are metallicity-dependent. For example, Leitherer & Heckman (1995) used evolutionary synthesis models for populations of massive stars to show that WR stars can appear after just 2.5 Myr in twice-solar populations and after just 2.0 Myr in solar populations. Eldridge et al. (2017) also examined the presence of WR stars by subclass and found that WC stars appear after 2.5 Myr in solar populations, in agreement with Leitherer & Heckman (1995), but that WN stars can appear slightly earlier after 2.0 Myr. If WR stars can appear after only 2 Myr, then, within the uncertainties, the stellar population ages for our sample allow for the presence of WRs. Only the SB99 age for Re-

gion 2 would be exceptional, but is also within agreement assuming an accuracy of < 1 Myr (Sirressi et al. 2022).

Alternatively, we could be observing a pre-WR phase of VMSs. The characteristic emission features used to identify WR stars arise in their dense, high-velocity stellar winds. Because VMSs also produce exceptionally strong stellar winds and have high mass loss rates, their spectra can mimic those of the later evolutionary stage of WRs (e.g., Martins et al. 2008; Gräfener & Hamann 2008). In general, the FUV spectra of VMSs and WRs are difficult to tell apart. Both VMSs and WRs have been observed to have many of the features present in our HST/COS spectra, including N IV] λ 1486, He II λ 1640, and N IV λ 1720 (e.g., Martins & Palacios 2022). On one hand, Martins et al. (2023) argue that the UV alone is insufficient and the optical WR feature morphologies are needed to distinguish between VMSs and WRs. As such, the presence of the blue bump in some of our spectra favors the presence of WR stars. On the other hand, VMSs are only present at very young stellar population ages (< 2.5 Myr), suggesting VMSs could be the source of the excess wind profiles in our spectra and the corresponding young ages of the SB99 fits.

The ionizing stellar populations in M101 could contain a complicated mixture of massive stars with a range of ages (< 10 Myr) such that both VMSs and WRs are present. However, the presence of VMSs alone is deemed unlikely. First, the presence of Si IV P-Cygni profiles in Regions 1 and 2 in Figures 2 and 3 require older ages than what is physical for VMSs (e.g., Crowther et al. 2016; Smith et al. 2016). Additionally, the presence of O V λ 1371 is considered a key spectral diagnostic of VMSs, but there are no strong detections in the M101 spectra. The observed spectrum of Region 1 in Figure 3 shows weak O V absorption, indicating that VMSs may also be present in this region. However, the other regions show either no absorption at O V λ 1371 or blue-shifted absorption that is more consistent with Fe V λ 1365. For the other WR spectra (Regions 2, 6, 7, and 8) in Figure 3, the ambiguous absorption feature near $\lambda 1370$ is well fit by the Fe V feature in the stellar continuum model. Therefore, WRs seem to be the dominant wind source in our spectra, although we cannot Further, such large, complex H II regions as are seen in M101 might be likely places to find multiple, unresolved stellar populations hosting both WRs and VMS.

Proving the presence of strong WR stars at moderate metallicities is also challenging because WR features have not been observed in the spectra of individual metal-poor massive stars. This may simply be due to the fact that metal-driven winds in the photospheres of massive stars decrease with lower metallicities by definition. As a result, WR features have also proven difficult to produce in theoretical models at low metallicities, while WR features appear at relatively high metallicities and progressively increase in

strength (e.g., broad He II emission) in the stellar population synthesis models. Therefore, the presence of WR features in our observed spectra may be driving our best continuum fits to higher luminosity-weighted metallicities. In turn, requiring high metallicities to fit the WR features may drive the luminosity-weighted ages younger. This could explain the large offset in BPASS stellar metallicity in Figure 7 for the subset of H II regions with WR features in their spectra.

The WN-type stars in our M101 H II region sample are further confirmed by their relatively large N/O abundances in Table 2 (larger for WR regions than non-WR regions) and their FUV N spectral features. As mentioned in Section 4, WR stars may also be responsible for the N IV] $\lambda\lambda 1483,1487$ emission and excess emission in the N IV λ 1719 P-Cygni profile are seen in Figures 2 (also see Figure 4). Such N IV] detections are very intriguing. First, N IV] $\lambda\lambda 1483,1487$ emission is rare and has only been reported for a handful of galaxies and active galactic nuclei (AGN) across all redshifts. Second, there has been heightened interest in N IV] due to its strong detection in the JWST/NIRSpec spectrum of the exceptionally bright z = 10.6 galaxy GN-z11 (Bunker et al. 2023). As a result, WR stars have been suggested as a source of increased N emission for GN-z11 and other galaxies (e.g., Senchyna et al. 2023).

The WR-driven N features seen in our M101 spectra are further supported by the presence of P-Cygni profiles of the resonance or excited transitions of metal lines in bluest portions of the FUV spectra, including S VI $\lambda\lambda$ 933,945, N IV λ 955, N III λ 991, O VI $\lambda\lambda$ 1032,1038, P V $\lambda\lambda$ 1118,1128, and C III λ 1175. This combination of features and range of moderate- to high-ionization potential species is consistent with the later WN6-WN7 *FUSE* spectra described in Willis et al. (2004). Additionally, if WC stars were present, we'd expect to see strong emission or P-Cygni profiles of C III $\lambda\lambda$ 977,1140 and/or C IV $\lambda\lambda$ 1107,1135,1169, yet we see no evidence of significant WC stars in the blue segment of our FUV spectra.

5.4. Impact of WR Stars on Inferred Stellar Properties

While our integrated FUV spectra are difficult to fit with current stellar models owing to the complex blend of massive star and WR contributions, it is clear that the WR features can have a significant impact on stellar continuum and subsequently derived properties. The impact of WR stars on integrated star-forming spectra can be seen in the residuals to our stellar population model fits. The spectral regions where our stellar population synthesis fits perform the poorest correspond to underfit WN P-Cygni and emission profiles (e.g., N IV λ 1720), suggesting that the SB99 and BPASS models fail to reproduce the full WR populations in these observed regions. Fortunately, the Potsdam Wolf-Rayet (PoWR; Sander et al. 2015; Todt et al. 2015) model atmo-

14 BERG ET AL.

spheres for WR stars can provide significantly better fits to the FUV WN features. In the yellow window of Figure 3 we expand the observed spectrum of Region 1 around the N III λ 991 feature and overplot a stellar model from the PoWR MW WNL-H20 grid that corresponds to $T_{\star}=50.1$ kK and log $(R_t/R_{\odot})=0.3$. After a relative scaling between spectra, it is clear that the N III λ 991 emission is easily reproduced by a WN star. Therefore, the observed spectra require a combination of ordinary massive stars and WN stars to full fit it.

On the other hand, the WN features discussed in this work can provide powerful tools to improve our interpretation of FUV continuum spectra. Using our M101 FUV spectra, we have demonstrated that the $\sim 900-1200$ Å stellar continuum features provide strong diagnostics of the presence of WR stars that can be used to interpret the integrated spectra of star-forming regions or galaxies. Further, these very blue spectra provide support for the presence of WN stars as the source of excess N IV $\lambda\lambda 1483,1486$ and N IV $\lambda 1720$ emission. As discussed above, the presence of very high ionization stellar wind profiles suggests the presence of veryhot / young massive stars, whose integrated spectra are better characterized by the SB99 and BPASS models. However, the SB99 and BPASS models either do not have sufficient numbers of WR stars or do not include appropriate WR evolutionary tracks to reproduce the excess N emission observed in our spectra. As a result, in trying to fit this excess emission, the SB99 model fits are biased to higher-metallicities and younger ages. Therefore, the H II regions of M101 provide excellent benchmarks for constraining the revised inclusion of WR and VMS stars in stellar population models. As such, we provide the emission-line properties for important UV and optical WR features measured for Regions 1 and 2 in Table 4.

5.5. O III] and C III] Emission

The FUV O III] $\lambda\lambda$ 1661,1666 and C III] $\lambda\lambda$ 1907,1909 nebular emission lines offer the opportunity to investigate the relative C/O abundance in galaxies. In general, carbon abundance determinations in extragalactic H II regions are rare in the literature due to the lack of bright CELs of C in the optical and the extreme faintness of the optical RLs. Previous C/O studies have been most successful in measuring the UV C and O CELs in metal-poor dwarf galaxies (12+ $\log(O/H)$ < 8.0); e.g., Garnett et al. 1995; Berg et al. 2016, 2019a), while optical RL studies dominate in metal-rich regions (12+log(O/H) > 8.0) of very nearby galaxies (e.g., Peimbert et al. 2005; Bresolin 2007; Esteban et al. 2009; Esteban et al. 2014; Toribio San Cipriano et al. 2016, 2017). Given this apparent dichotomy in the previous C/O measurements, comparisons between the CEL and RL methods for C/O have remained sparse.

Table 4. Stellar Wind Emission-Line Properties

	Region 1			Region 2			
Line	EW FWHM (Å) (km s ⁻¹)			EW (Å)	FWHM (km s ⁻¹)		
N IV] λ1486	-1.37	1434		-0.72	862		
He II $\lambda 1640$	-2.77	1436		-3.08	1344		
N IV $\lambda 1720$	-1.08	603		-1.54	636		
? $\lambda 1726$	-0.77	603		-0.81	636		
N III λ 4634	-0.99	950		-1.78	936		
N III $\lambda 4640$	-2.00	1085		-2.36	748		
C III $\lambda 4650$	-0.33	345		-0.57	294		
He II $\lambda 4686$	-3.20	975		-8.99	1586		
C IV λ 5801	-0.55	775		-0.27	362		
C IV $\lambda 5808$	-0.55	775		-0.38	362		

	He II $\lambda 1640$		He II	$\lambda 4686$
	EW	FWHM	EW	FWHM
	(Å)	$(km s^{-1})$	(Å)	$(km s^{-1})$
Region 1	-2.77	1436	-3.20	975
Region 2	-3.08	1344	-8.99	1586
Region 4	_	_	_	_
Region 5	-1.81	742	_	_
Region 6	-2.05	1113	-3.73	1202
Region 7	-2.62	1981	-3.52	1574
Region 8	-3.34	1666	-3.36	1201
Region 9	-1.02	859	-0.68	289
Region 10	-1.95	1420	-1.31	296

NOTE— Emission-line properties of stellar wind features observed in the UV and optical spectra of the M101 sample. *Top:* Line fits for the regions with the strongest wind features (Regions 1 and 2). Column 1 lists the ion and wavelength of each emission line, with the exception of the emission feature near $\lambda 1726$ that has an uncertain association. Columns 2 and 3 list the equivalent width (EW) and Gaussian full width half maximum (FWHM) for Region 1, while Columns 4 and 5 list EW and FWHM for Region 2. *Bottom:* UV and optical He II emission properties for the full sample. Note that the He II features are not well fit in the low-resolution UV spectra for regions with weak emission (EW $_{\lambda 1640}$ < 2Å).

Optical measurements of abundances in metal-rich H II regions ($12+\log(O/H) > 8.0$) typical of spiral galaxies are difficult in general. Since the cooling in H II regions is dominated by IR fine-structure lines of N⁺⁺ and O⁺⁺ for high metallicities, the greater the metallicity, the greater the cooling. The lower electron temperatures mean that the higher excitation CELs become progressively weaker, and the electron temperature becomes difficult to measure. This is a problem especially for C, as the main ionization state, C⁺⁺, has its strongest emission in the UV, and this becomes vanishingly faint in metal-rich nebulae.

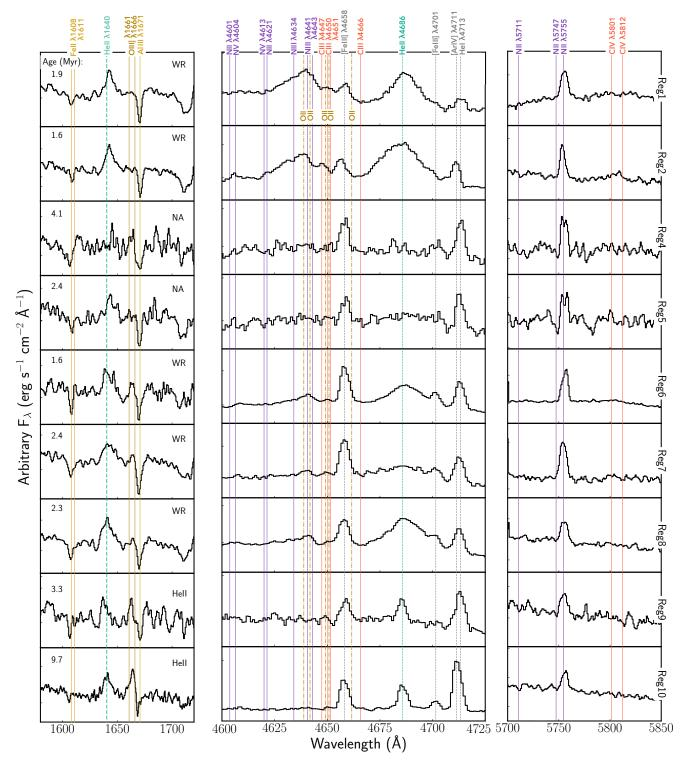


Figure 8. Comparison of FUV He II emission features (*left panel*) with the optical WR blue bump (*middle panel*) and red bump (*right panel*) features. We detect strong blue WR features in several of the regions, indicating the presence of nitrogen-type WR (WN) stars. Regions identified by Croxall et al. (2016) to have narrow, nebular He II emission or WR emission in their optical spectra are labeled accordingly in the upper right-hand corner of the left-panel plots. We do not detect any red bumps in the right panel, and thus lack explicit evidence of carbon-type WR (WC) stars, but there may be C III contributions to the blue bump in the middle panel.

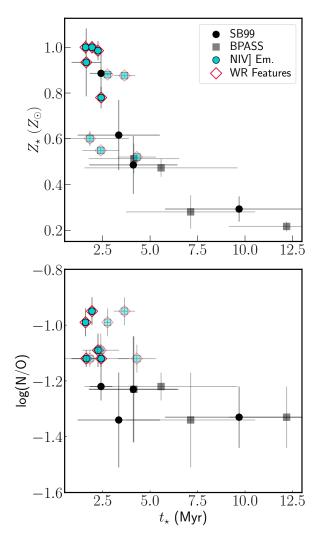


Figure 9. *Top:* Modeled luminosity-weighted metallicity versus age for the ionizing stellar populations in our H II region sample. We show points derived using both SB99 (circles) and BPASS (semitransparent squares) models. Regions with WR features in their optical spectra are outlined by a red diamond; these regions also have N IV emission in their FUV spectra (turquoise points). H II regions with WR features only occupy the upper left young-age, high-metallicity regime of the plot. *Bottom:* N/O abundance measured from the optical spectra versus modeled stellar age shows that the same regions that have enhanced N/O gas abundances have enhanced N IV] emission and strong WR features in their spectra. This supports the idea that the WR phase is responsible for the observed local N enhancement in these H II regions.

Due to these challenges, there is a paucity of metal-rich targets with significant UV C III] and O III] detections. For example, Garnett et al. (1999) observed C III] in 4 metal-rich H II regions in the spiral galaxies NGC 2403 and M101 using FOS/HST, but were unable to obtain any significant detections of the O III] doublet. Because COS is significantly more sensitive than FOS, HST is now better able to detect the

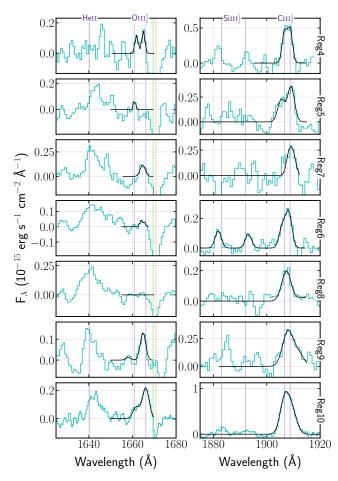


Figure 10. Continuum-subtracted *HST*/COS spectra of the seven H II regions with C III] $\lambda\lambda 1907,1909$ emission. Monte-Carlo minimization fits to the Gaussian profiles of O III] and C III] are shown as black lines. Many of the O III] profiles lack sufficient signal due to the neighboring Al II $\lambda 1671$ ISM (orange dashed line) and MW (green dashed line) absorption profiles.

C III] and O III] UV emission lines in metal-rich H II regions, such as the two regions with $12+\log(O/H) > 8.2$ reported in Senchyna et al. (2017).

5.5.1. Flux Measurements

The O III] $\lambda\lambda 1661,1666$ and C III] $\lambda\lambda 1907,1909$ emission line features of our UV *HST/COS* spectra are plotted in Figure 10. To determine the emission line strengths for these UV features, we first continuum-subtracted the spectra using the best-fit stellar continua described in Section 5.1. The UV emission lines were then fit using the scipy.optimize.curve_fit (Virtanen et al. 2020) to perform a least-squares minimization on the built-in Gaussian function in the lmfit python package (Newville et al. 2018). Groups of nearby lines were fit simultaneously, constrained by a single Gaussian FWHM and a single line center offset from the vacuum wavelengths (i.e., redshift). Fig-

ure 10 shows the Gaussian fits to the significant O III] and C III] emission lines in the COS spectra of M101.

The errors of the flux measurements were approximated using

$$\sigma_{\lambda} \approx \sqrt{(2 \times \sqrt{N} \times \text{RMS})^2 + (0.01 \times F_{\lambda})^2},$$
 (1)

where N is the number of pixels spanning the Gaussian profile fit to the emission lines. The root mean squared (RMS) noise in the continuum was taken to be the average of the RMS on each side of an emission line when free of absorption features. The two terms in Equation 1 approximate the errors from continuum subtraction and flux calibration, where the flux calibration uncertainty is assumed to be 1% of the flux based on the standard star calibrations in CALSPEC (Bohlin 2010). For weak lines, such as the UV CELs, the RMS term determines the approximate uncertainty. Finally, UV fluxes and errors were corrected for extinction using the reddening law of Reddy et al. (2016) and nebular color excesses (E(B-V)) derived from the optical Balmer lines from Croxall et al. (2016). The reddening corrected line intensities measured for our C/O targets are reported in the top of Table 5.

Seven of our 10 targets have significant C III] detections, which we consider a high success rate given the relatively large O/H abundances of our sample. However, only one region has a significant O III] detection. For nearby galaxies at redshifts close to 0.003, it is possible for the O III] $\lambda 1666$ to be significantly affected by absorption from the Galactic Al II $\lambda 1671$ line (see, e.g., the UV spectrum of SB191 in Senchyna et al. 2017). M101 has a redshift of $z \approx 0.0008$ such that the O III] $\lambda 1666.15$ emission line shifts to a line center of 1667.48 Å, but O III] can be further shifted towards Al II contamination by the rotational velocity of a given H II region within M101. These effects, combined with the low resolution of our spectra, cause the Al II absorption to significantly affect the O III] profile. The resulting effect is clearly seen in Figure 10: the O III] line strengths are weak for most of the sample, where the blue Al II absorption wing is clearly blended with the O III] emission. Therefore, higher resolution spectra are needed to strongly detect the FUV O III] nebular emission in M101 and other metal-rich targets.

5.5.2. The C/O Abundance Ratio

Determining relative abundances requires significant ($>3\sigma$) line detections. While several of our C III] line detections meet this criteria, only Region 10 has a significant O III] detection. We, therefore, perform C/O abundance determinations only as an exploratory exercise, noting that higher S/N and higher resolution spectra are needed for robust measurements. Given the faint hints of O III] emission in Regions 9, 7, 6, and 4, significant detections could likely be achieved with higher spectral resolution. We note that we

refrain from performing a 1-sigma upper limit calculation because the contamination of the MW Al II $\lambda 1671$ absorption feature would lead to an underestimation of the upper limit.

To perform an exploratory C/O abundance analysis, an initial approximation of C/O can be determined from the C⁺²/O⁺² ratios reported in Table 5. However, the higher ionization potential of O⁺² relative to C⁺² (54.9 eV versus 47.9 eV, respectively), means that an ionization correction factor is needed to account for any unseen ionization states. For the spectra shown in Figure 2, the C IV emission features all seem to be well fit by a stellar wind P-Cygni profile, suggesting that we are not missing any significant emission from C⁺³ ions. However, there could be contributions from lower ionization states. Therefore, we determine C/O abundances using:

$$\frac{C}{O} = \frac{C^{+2}}{O^{+2}} \times \left[\frac{X(C^{+2})}{X(O^{+2})} \right]^{-1}$$

$$= \frac{C^{+2}}{O^{+2}} \times C \text{ ICF}, \tag{2}$$

where $X(C^{+2})$ and $X(O^{+2})$ are the C^{+2} and O^{+2} volume fractions, respectively. Following the metallicity-dependent ICF method of Berg et al. (2019a), we ran CLOUDY 17.00 (Ferland et al. 2013) photoionization models to match the properties spanned by M101. We used BPASS burst models for the input ionizing radiation field, a range of burst ages $(10^{6.0}-10^{7.0})$ yrs), ionization parameter $(-3.0 < \log U < -1.0)$, and metallicities $(Z=0.004-0.02=0.2-1.0 \ Z_{\odot})$, with matched stellar and nebular metallicities $(Z_{\star}=Z_{neb})$.

Our CLOUDY models are shown in Figure 11 comparing the [O III] $\lambda 5007/[O II] \lambda 3727$ emission line ratios, ionization parameters, and ionization fractions of C^{+2} and O^{+2} . The top panel shows the increasing trend of [O III] λ 5007/[O II] $\lambda 3727$ with ionization parameter, which is a useful diagnostic. The points are color-coded by model stellar/nebular metallicity, while the shaded band denotes the corresponding models spanned by the range in burst age. We fit each of the metallicity models with a polynomial of the shape: $\log U = c_3 \cdot x^2 + c_2 \cdot x + c_1$, where $x = \log([O III] \lambda 5007/[O II])$ λ 3727). The coefficients for these fits are listed in Table 6. We note that the coefficients derived in this work are slightly different than those reported in Berg et al. (2019a) for common metallicities because we took the average values of the models spanning different ages, while the previous work fit the $t = 10^{6.5}$ yr models only. Using the observed [O III] λ 5007/[O II] λ 3727 ratios from Croxall et al. (2016) and the metallicities reported in Berg et al. (2020), we determined log U values by interpolating between the polynomial fits defined for each metallicity steps; the resulting values are reported in Table 5.

With log U estimates in hand, we determined C ICFs for our sample. As shown in the middle panel of Figure 11, both metallicity and stellar age have moderate effects on the relative ionization fraction of C. We fit each of the metallicity models with a polynomial of the shape: C ICF = $[X(C^{+2})/X(O^{+2})]^{-1} = c_5 \cdot x^4 + c_4 \cdot x^3 + c_3 \cdot x^2 + c_2 \cdot x + c_1$, where $x = \log U$. The coefficients for these fits are listed in Table 6. We determined moderate C ICFs for our sample, showing a moderate to small correction for our sample that lies between $\log U = -2.75$ to -2.30. We estimated the uncertainty in the ICF as the scatter amongst the different models considered (relative abundances and burst age) at a given $\log U$. Ionization parameters, C ICFs, ionic C fractions, and corrected C/O ratios are provided in Table 5.

The bottom panel of Figure 11 shows the ionization fraction of $C^{+2}/(C^++C^{+2})$ vs $O^{+2}/(O^++O^{+2})$. If the singly- and doubly-ionized species are the dominant species of C and O, then these ratios can be used directly as an independent ICF. Using the $O^{+2}/(O^++O^{+2})$ ratio derived from the optical spectra, we predict the $C^{+2}/(C^++C^{+2})$ ratios for our sample. The C^{+2}/C ICF values are report in Table 5. Compared to the our C ICFs derived from the ionization parameter, the C^{+2}/C ICF values are always lower and less than one, which would provide a more significant correction to our C/O abundances.

Note that the C and O abundances presented here have not been corrected for the fraction of atoms embedded in dust. Peimbert & Peimbert (2010) have estimated that the depletion of O ranges between roughly 0.08-0.12 dex, and has a positive correlation with O/H abundance. C is also expected to be depleted in dust, mainly in polycyclic aromatic hydrocarbons and graphite. The estimates of the amount of C locked up in dust grains in the local interstellar medium shows a relatively large variation depending on the abundance determination methods applied (see, e.g., Jenkins 2014). However, carbon and oxygen are often found to have similar amounts of depletion onto dust grains, with corrections typically around 0.1 dex (e.g., Esteban et al. 1998; Jenkins 2009). Assuming the C and O depletions are similar, we take the gas-phase C/O ratio as indicative of the total C/O abundance for this exercise.

5.5.3. C/O Comparison to Previous Works

Several previous studies have analyzed the nebular abundances in M101. Of these studies, four are particularly relevant to this work: (1) Garnett et al. (1999) observed three H II regions in M101 using the Faint Object Spectrograph (FOS) on HST. C III] $\lambda\lambda$ 1907,1909 was detected significantly in all three, but only upper limits could be placed on O III] $\lambda\lambda$ 1661,1666. As tabulated in Table 7, two of

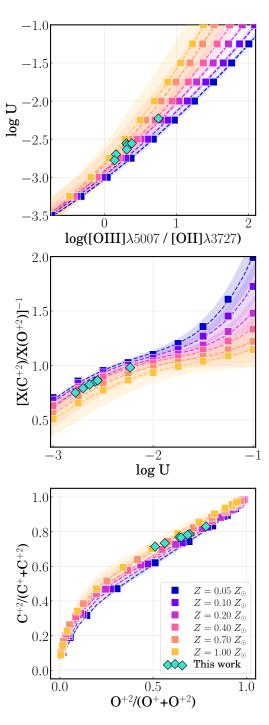


Figure 11. Photoionization models used to derive the carbon ICF. Models with $t = 10^{6.5}$ yrs are plotted as squares and color-coded by their metallicity. The best-fit polynomial function for each metallicity is plotted as a dashed line; fit coefficients are reported in Table 6. The range of models spanned by ages of $t = 10^{6-7}$ yrs are designated by the shaded bands, representing an estimate of the uncertainty. *Top:* Ionization parameter, $\log U$, as a function of the [O III] $\lambda 5007/[O II] \lambda 3727$ emission line ratio. *Middle:* Carbon ionization correction factor, CICF = $[X(C^{+2})/X(O^{+2})]^{-1}$, as a function of $\log U$. *Bottom:* Another CICF, $C^{+2}/(C^{+}+C^{+2})$, but derived as a function of the observed $O^{+2}/(O^{+}+O^{+2})$ ion fraction. The observed line ratios and ion fractions from Croxall et al. (2016) and derived $\log U$ and ICF values are plotted as teal diamonds.

Table 5	C/O	Emission	Line and	Abundance	Fetimates

Property	Reg 4	Reg 5	Reg 6	Reg 7	Reg 8	Reg 9	Reg 10
<i>I</i> (O Ⅲ])/ <i>I</i> (C Ⅲ])	0.144 ± 0.129	0.078 ± 0.253	0.163 ± 0.162	0.073 ± 0.177	0.192 ± 0.328	0.198 ± 0.233	0.183 ± 0.014
E(B-V)	0.185	0.093	0.042	0.180	0.070	0.049	0.231
$T_e[O III](K)$	9540 ± 90	9180 ± 90	9440 ± 70	9300 ± 70	9580 ± 80	10690 ± 90	12790 ± 170
C^{+2}/O^{+2}	0.21 ± 0.68	0.36 ± 0.50	0.18 ± 0.24	0.48 ± 0.44	0.16 ± 0.44	0.17 ± 0.28	0.23 ± 0.10
$log O_{32}$	0.16 ± 0.02	0.31 ± 0.01	0.32 ± 0.01	0.14 ± 0.01	0.38 ± 0.01	0.31 ± 0.01	0.75 ± 0.02
$\log U$	-2.70 ± 0.09	-2.56 ± 0.10	-2.58 ± 0.09	-2.78 ± 0.08	-2.55 ± 0.08	-2.64 ± 0.06	-2.23 ± 0.06
C ICF	0.791	0.862	0.851	0.750	0.862	0.824	0.981
C ⁺² /C ICF	0.714	0.768	0.785	0.734	0.781	0.766	0.830
log(C/O)	-0.79 ± 0.63	-0.51 ± 0.87	-0.81 ± 0.36	-0.45 ± 0.67	-0.87 ± 0.58	-0.85 ± 0.43	-0.65 ± 0.16
log(N/O)	-1.23 ± 0.19	-1.22 ± 0.05	-1.12 ± 0.03	-1.12 ± 0.05	-1.09 ± 0.06	-1.34 ± 0.17	-1.33 ± 0.11
12+log(O/H)	8.51 ± 0.10	8.51 ± 0.02	8.45 ± 0.02	8.39 ± 0.01	8.36 ± 0.02	8.29 ± 0.06	8.16 ± 0.02

NOTE— The top three rows give the reddening-corrected intensities of O III] and C III] from the UV spectra relative to $H\beta$ from the optical spectra, determined using the E(B–V) reddening reported in Croxall et al. (2016). Note that the O III] flux is just the strong line of the doublet, the λ 1666 feature, but the C III] flux is the total of the $\lambda\lambda$ 1907,1909 lines. The bottom portion of the table lists the physical properties derived for the gas, where optical-only properties are reported from Croxall et al. (2016) and Berg et al. (2020), and UV-derived properties are from this work. Only Region 10 has significant detections of both O III] and C III]; values for the other six regions are only estimates and are italicized to denote this.

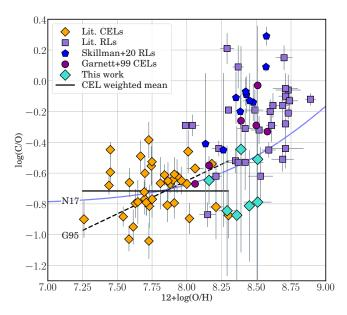


Figure 12. Carbon to oxygen ratio versus oxygen abundance for star-forming galaxies and H II regions. Low-metallicity galaxies with CEL C/O measurements from the literature (Berg et al. 2016; Senchyna et al. 2017; Berg et al. 2019b) are plotted as gold diamonds. Some additional CEL C/O abundances are plotted for individual H II regions from Garnett et al. (1999). We also include RL C/O abundances measured for higher-metallicity H II regions from Esteban et al. (2009); Esteban et al. (2020, purple squares) and Skillman et al. (2020, blue pentagons). The dashed line is the least-squares fit from Garnett et al. (1995), while the blue curve shows the empirical stellar curve from Nicholls et al. (2017). Some of our preliminary CEL C/O measurements (turquoise diamonds) agree with the overall increasing C/O–O/H trend, while others appear to be low-C/O outliers, but are not significant enough to discern from the large scatter.

Table 6. Coefficients for ICF Model Fits

	$Z(Z_{\bigodot})$							
y = f(x)	0.05	0.10	0.20	0.40	0.70	1.00		
$\log U$:								
$x = \log O_{32}$								
c3	0.0798	0.0899	0.1045	0.1308	0.1592	0.1938		
c ₂	0.7253	0.7514	0.7932	0.8588	0.9462	1.0290		
c_1	-3.026	-2.978	-2.914	-2.914	-2.836	-2.801		
C ICF:								
$x = \log U$								
C5	0.127	0.111	0.098	0.081	0.070	0.056		
c4	1.373	1.173	1.001	0.815	0.671	0.528		
c ₃	5.298	4.389	3.558	2.807	2.190	1.643		
c ₂	9.070	7.267	5.575	4.246	3.151	2.286		
c ₁	7.023	5.681	4.415	3.520	2.792	2.264		

NOTE— CLOUDY photoionization model fits of the form $f(x) = c_5 \cdot x^4 c_4 \cdot x^3 + c_3 \cdot x^2 + c_2 \cdot x + c_1$. The model grid and polynomial fits are shown in Figure 11. The models are described in § 5.5.2.

these regions overlap with our H II region sample in M101 (NGC5455, NGC5471). (2) Esteban et al. (2009) obtained high-resolution optical spectroscopy with the High Resolution Echelle Spectrometer (HIRES; Vogt et al. 1994) on the Keck I telescope for two H II regions in M101 and intermediate-resolution spectroscopy of NGC 5447 using the Intermediate dispersion Spectrograph and Imaging System (ISIS) spectrograph on the 4.2m WHT. They measured significant C II RLs in H1013 and NGC 5447b, which overlaps with our UV CEL measurement. (3) Skillman et al. (2020) measured significant C II RLs in 10 H II regions in M101 using low-resolution optical spectroscopy taken with the MODS on the LBT. (4) Esteban et al. (2020) used lowresolution optical spectroscopy taken with the Optical System for Imaging and low-Intermediate-Resolution Integrated Spectroscopy (OSIRIS; Cepa et al. 2000) spectrograph on the Gran Telescopio Canarias (GTC) to measure the RLs in 11 H II regions in M101, five of which have significant C II. Of these regions, NGC 5455 and NGC 5471 are in common with

Garnett et al. (1999), Skillman et al. (2020), and this work, NGC 5447b is in common with Esteban et al. (2009), Skillman et al. (2020), and this work, H1013 overlaps with the Skillman et al. (2020) sample, while H37 has no comparison. These previous works provide consistency checks on our measurements.

We conduct a preliminary comparison of our UV C/O abundance measurements to previous studies in the C/O versus O/H plot in Figure 12. In general, the study of the C/O versus O/H trend is of interest to improve our understanding of C production and the conditions in which C emission is strongest (e.g., high-redshift star-forming regions). Theoretically, we expect C/O nucleosynthetic production to be constant via the triple- α process. However, observationally an increasing trend in C/O with O/H is clearly visible, but with significant scatter. This dispersion has prevented us from further discerning whether C/O increases linearly or gradually with O/H (e.g., the dashed line from Garnett et al. (1995) or solid blue line from Nicholls et al. (2017) in Figure 12) or has a bimodal trend with a plateau at low O/H, similar to the N/O trend.

A further challenge to understanding the C/O-O/H relationship is the differing sources of C/O measurements; at low-metallicity C/O is measured via the collisionally-excited UV lines, while C/O is typically measured via the optical RLs at high-metallicity. Therefore, our measurements, combined with the CEL measurements from Garnett et al. (1999), provide an important extension of the CEL measurements at low-metallicity that would allow an apples-to-apples assessment of the C/O-O/H trend if more significant measurements were obtained. Along these lines, our measurements agree well with the dispersion of the C/O trend in Figure 12, but also lie at low C/O ratios on average. In particular, the low-metallicity (gold diamonds) plateau has an average $log(C/O)_{CEL} = -0.71$, while the high-metallicity average (Garnett et al. (1999) plus this work) $log(C/O)_{CEL} = -0.54$. Note that this value could be largely biased by the low average of our seven points ($log(C/O)_{CEL,B24} = -0.70$), whereas the Garnett et al. (1999) sample alone has a much higher average $(\log(C/O)_{CEL,G99} = -0.36)$. In comparison, the highmetallicity average $log(C/O)_{RL} = -0.29$, or roughly 0.1 dex higher than previous CEL C/O measurements, and much higher than the values estimated here. Despite the large uncertainties that remain, these results suggest that (1) the increasing C/O trend is real and not just an artifact of different measurement methods and (2) that a C/O abundance discrepancy factor (ADF) exists on the same order of magnitude, or larger, as the O/H ADF. However, little more can be said given the large uncertainties on our C/O measurements. Further progress to improve comparison of C/O from the UV CELs to those from optical RLs and better constrain

the source(s) of the ADF will require higher S/N and higher spectral-resolution spectra.

6. CONCLUSIONS

We present low-resolution *HST/COS* FUV spectroscopy of 9 H II regions in the star-forming disk of spiral galaxy M101. These regions were selected for their high surface brightnesses and existing direct abundances and C II λ 4267 RL detections from the optical CHAOS survey, with the goal of detecting the FUV O III] λ 1666 and C III] $\lambda\lambda$ 1907,1909 CELs. Strong C III] emission lines were detected for the 7 lowest-metallicity H II regions in our sample (12+log(O/H) \lesssim 8.5), but O III] λ 1666 was significantly detected in only the most metal-poor region (Reg 10; 12+log(O/H) = 8.16). The other six H II regions have tentative O III] detections that would be improved with higher spectral resolution due to the narrow intrinsic widths of the lines and the contamination of the Milky Way Al II λ 1671 ISM absorption line.

We performed an exploratory C/O abundance analysis with the limited O III] and C III] line detections. To convert the C/O emission line ratios to relative abundances, we produced new analytic functions of the carbon ICF as a function of metallicity that are calibrated to the conditions of the M101 H II regions. To do so, we created a custom grid of CLOUDY photoionization models using BPASS single-burst models as inputs. With our tentative C/O abundance measurements, we compared to the existing sample of C/O measurements for M101, consisting of 17 optical RL measurements and 3 FUV CEL measurements for 11 different H II regions (see Table 7). Our preliminary C/O measurements add 7 CEL points to this sample, but five of these points our low C/O outliers from the general C/O-O/H trend (Figure 12). While the FUV C/O abundances can provide useful constraints on the chemical enrichment of galaxies, higher-S/N and higherresolution CEL measurements are clearly needed to robustly constrain the high-metallicity end of the C/O-O/H and compare to RL C/O abundances.

Despite the lack of strong O III] CELs, the resulting FUV spectra revealed numerous continuum features, such as the massive-star wind features, that are useful for characterizing the ionizing stellar population. We fit stellar continuum with both SB99 and BPASS luminosity-weighted stellar burst models to determine the characteristic age and metallicity of the massive star populations, finding a range of ages (2–10 Myr) and metallicities $(0.5-1.0~Z_{\odot})$ that seem to correlate with the He and N emission and P-Cygni profiles observed. In particular, the youngest stellar populations are strongly correlated with broad Wolf-Rayet (WR) He II λ 1640 emission and enhanced N/O abundances (log(N/O)> -1.2), as determined from the optical [N II] λ 6584/[O II] λ 3727 ratio.

Table 7. Comparison of M101 CEL and RL C/O Measurements

Name	e	R.A., Decl.	12+log(O/H)	log(C/O)	Method	Source
H1013 ¹	Reg 1	14:03:31.3, +54:21:05.8	8.57 ± 0.02	-0.04 ± 0.07	RL	Skillman et al. (2020)
		14:03:31.2, +54:21:14.8		$+0.22 \pm 0.13$	RL	Esteban et al. (2009)
H1052 ¹	Reg 2	14:03:34.1, +54:18:39.6	8.57 ± 0.01	-0.08 ± 0.04	RL	Skillman et al. (2020)
NGC 5461	Reg 3	14:03:41.6, +54:19:08.5	8.48 ± 0.02	-0.31 ± 0.12	RL	Skillman et al. (2020)
		14:03:41.6, +54:19:04.4		-0.03 ± 0.13	CEL	Garnett et al. (1999) ²
NGC 5462a	Reg 4	14:03:53.0, +54:22:06.8	8.45 ± 0.05	-0.39 ± 0.19	RL	Skillman et al. (2020)
	_			-0.79	CEL	This work
NGC 5462b	Reg 5	14:03:53.8, +54:22:10.8	8.43 ± 0.01	-0.28 ± 0.12	RL	Skillman et al. (2020)
				-0.51	CEL	This work
		14:03:53.1, +54:22:06.4		-0.12 ± 0.10	RL	Esteban et al. (2020)
NGC 5447	Reg 6	14:02:30.5, +54:16:09.9	8.42 ± 0.01	-0.30 ± 0.09	RL	Skillman et al. (2020)
				-0.81	CEL	This work
NGC 5455	Reg 7	14:03:01.1, +54:14:28.0	8.39 ± 0.02	-0.34 ± 0.11	RL	Skillman et al. (2020)
				-0.45	CEL	This work
		14:03:01.2, +54:14:27.0		-0.26 ± 0.14	CEL	Garnett et al. (1999) ²
		14:03:01.2, +54:14:29.4		-0.22 ± 0.11	RL	Esteban et al. (2020)
NGC 5447	Reg 8	14:02:27.8, +54:16:25.3	8.35 ± 0.01	-0.25 ± 0.17	RL	Skillman et al. (2020)
				-0.87	CEL	This work
		14:02:28.7, +54:16:25		-0.15 ± 0.12	RL	Esteban et al. (2009)
		14:02:28.1, +54:16:26.9		-0.27 ± 0.11	RL	Esteban et al. (2020)
H37 ¹		14:02:17.7, +54:22:34.1	8.30 ± 0.01	-0.14 ± 0.14	RL	Esteban et al. (2020)
H1216 ¹	Reg 9	14:04:10.9, +54:25:19.2	8.26 ± 0.03	-0.63 ± 0.50	RL	Skillman et al. (2020)
				-0.85	CEL	This work
NGC 5471	Reg 10	14:04:29.0, +54:23:48.6	8.14 ± 0.03	-0.47 ± 0.46	RL	Skillman et al. (2020)
				-0.65 ± 0.16	CEL	This work
		14:04:29.0, +54:23:48.8		-0.67 ± 0.05	CEL	Garnett et al. (1999) ²
		14:04:29.0, +54:23:49.0		-0.20 ± 0.11	RL	Esteban et al. (2020)

NOTE— Comparison of M101 CEL C/O abundances to RL C/O abundances from the literature and this work. Column 1 lists the common name of the H II region in M101, along with the region name of this work, while coordinate R.A. and Decl. (J2000) is given in Column 2. Column 3 lists the measured 12+O/H abundances from Croxall et al. (2016), while Column 4 lists the C/O abundance measured using the method in Column 5 by the reference in Column 6. Note that estimates of log(C/O) using insignificant detections on O III] in this work are identified with italicized values.

¹ Name adopted from the catalog of Hodge et al. (1990). ² Note that the values from Garnett et al. (1999) are those calculated

Detections of WR stars are further supported by visual confirmation of the WR "blue bump" feature around $\lambda 4650$ in the optical spectra, where the strong N II $\lambda\lambda 4634,4641,4643$ emission is indicative of nitrogen-type WR (WN) stars. As a result, this special phase of stellar evolution may be responsible for the N IV $\lambda\lambda 1483,1486$ emission and the excess emission in the N IV $\lambda 1718$ stellar wind feature, which in turn biases the SB99 and BPASS stellar continuum fits to higher metallicities relative to the gas-phase metallicities. Therefore, the WR H II regions of M101 presented here provide a strong test-bed to constrain future WR atmosphere and evolution models, and their incorporation to stellar population models

Finally, we observed additional P-Cygni and emission features in the $\sim 900-1200$ Å regime of our M101 spectra that further support strong contributions from WN stars (e.g., S VI $\lambda\lambda933,945,$ N IV $\lambda955,$ N III $\lambda991,$ O VI $\lambda\lambda1032,1038,$ P V $\lambda\lambda1118,1128,$ and C III $\lambda1175),$ and note a lack of strong C III and C IV features in this regime (e.g., C III $\lambda977,$ C IV $\lambda1197,$ C IV $\lambda1135,$ C III $\lambda1140,$ C IV $\lambda1169)$ that would be expected if WC stars were present. Therefore, we recommend the $\sim900-1200$ Å stellar continuum as a powerful

diagnostic regime for identifying the presence of WR stars in the integrated spectra of star-forming regions and galaxies.

Facilities: HST (COS), LBT (MODS)

Software: astropy (Astropy Collaboration et al. 2013, 2018, 2022), CalCOS (STScI), dustmaps (Green 2018), jupyter (Kluyver et al. 2016), LINMIX (Kelly 2007), MPFIT (Markwardt 2009), MODS reduction Pipeline, Photutils (Bradley et al. 2021), LMFIT version 1.2.2 (Newville et al. 2018), PyNeb version 1.1.14 (Luridiana et al. 2015), BPASS version 2.2 (Stanway & Eldridge 2018), Starburst99 (Leitherer et al. 2014), numpy version 1.26 (Harris et al. 2020)

¹Name adopted from the catalog of Hodge et al. (1990). ²Note that the values from Garnett et al. (1999) are those calculated with an R_V value of 3.1. Garnett et al. (1999) also calculated values assuming an R_V value of 5, which can give significantly different results.

The authors are grateful to the referee for insightful comments and questions that led to better parameter characterization and an overall improved paper. DAB is grateful for the support for this program, HST-GO-15126, that was provided by NASA through a grant from the Space Telescope Science Institute, which is operated by the Associations of Universities for Research in Astronomy, Incorporated, under NASA contract NAS5-26555. This work was based in part on observations made with the Large Binocular Telescope (LBT). The LBT is an international collaboration among institutions in the United States, Italy, and Germany. The LBT Corporation partners are: the University of Arizona on behalf of the Arizona university system; the Istituto Nazionale di Astrofisica, Italy; the LBT Beteiligungsgesellschaft, Germany, representing the Max Planck Society, the Astrophysical Institute Potsdam, and Heidelberg University; the Ohio State University; and the Research Corporation, on behalf of the University of Notre Dame, the University of Minnesota, and the University of Virginia. This research used the facilities of the Italian Center for Astronomical Archive (IA2) operated by INAF at the Astronomical Observatory of Trieste. This paper made use of the modsIDL spectral data reduction reduction pipeline developed in part with funds provided by NSF Grant AST-1108693 and a generous gift from OSU

REFERENCES

Abbott, D. C., & Conti, P. S. 1987, ARA&A, 25, 113, doi: 10.1146/annurev.aa.25.090187.000553

Arellano-Córdova, K. Z., Berg, D. A., Chisholm, J., et al. 2022, ApJ

Asplund, M., Amarsi, A. M., & Grevesse, N. 2021, A&A, 653, A141, doi: 10.1051/0004-6361/202140445

Astropy Collaboration, Price-Whelan, A. M., Lim, P. L., et al. 2022, ApJ, 935, 167, doi: 10.3847/1538-4357/ac7c74

Astropy Collaboration, Price-Whelan, A. M., Sipőcz, B. M., et al. 2018, AJ, 156, 123, doi: 10.3847/1538-3881/aabc4f

Astropy Collaboration, Robitaille, T. P., Tollerud, E. J., et al. 2013, A&A, 558, A33, doi: 10.1051/0004-6361/201322068

Beaton, R. L., Seibert, M., Hatt, D., et al. 2019, ApJ, 885, 141, doi: 10.3847/1538-4357/ab4263

Berg, D. A., Chisholm, J., Erb, D. K., et al. 2019a, ApJL, 878, L3, doi: 10.3847/2041-8213/ab21dc

Berg, D. A., Erb, D. K., Henry, R. B. C., Skillman, E. D., & McQuinn, K. B. W. 2019b, ApJ, 874, 93,

doi: 10.3847/1538-4357/ab020a

10.17909/qv80-ph56.

Berg, D. A., Pogge, R. W., Skillman, E. D., et al. 2020, ApJ, 893, 96, doi: 10.3847/1538-4357/ab7eab

Astronomy alumnus David G. Price through the Price Fel-

All the *HST* data used in this paper can be found in MAST:

lowship in Astronomical Instrumentation.

Berg, D. A., Skillman, E. D., Croxall, K., et al. 2015, ApJ, 806, 16Berg, D. A., Skillman, E. D., Henry, R. B. C., Erb, D. K., & Carigi, L. 2016, ApJ, 827, 126

Bohlin, R. C. 2010, AJ, 139, 1515

Bradley, L., Sipöcz, B., Robitaille, T., et al. 2021, astropy/photutils: 1.1.0, 1.1.0, Zenodo, doi: 10.5281/zenodo.4624996

Bresolin, F. 2007, ApJ, 656, 186

Bunker, A. J., Saxena, A., Cameron, A. J., et al. 2023, A&A, 677, A88, doi: 10.1051/0004-6361/202346159

Cameron, A. J., Katz, H., Rey, M. P., & Saxena, A. 2023, MNRAS, 523, 3516, doi: 10.1093/mnras/stad1579

Castor, J. I., Abbott, D. C., & Klein, R. I. 1975, ApJ, 195, 157, doi: 10.1086/153315

- Cepa, J., Aguiar, M., Escalera, V. G., et al. 2000, in Society of Photo-Optical Instrumentation Engineers (SPIE) Conference Series, Vol. 4008, Optical and IR Telescope Instrumentation and Detectors, ed. M. Iye & A. F. Moorwood, 623–631, doi: 10.1117/12.395520
- Charbonnel, C., Schaerer, D., Prantzos, N., et al. 2023, A&A, 673, L7, doi: 10.1051/0004-6361/202346410
- Chisholm, J., Rigby, J. R., Bayliss, M., et al. 2019, ApJ, 882, 182, doi: 10.3847/1538-4357/ab3104
- Crowther, P. A. 2007, ARA&A, 45, 177
- Crowther, P. A., Caballero-Nieves, S. M., Bostroem, K. A., et al. 2016, MNRAS, 458, 624, doi: 10.1093/mnras/stw273
- Croxall, K. V., Pogge, R. W., Berg, D. A., Skillman, E. D., & Moustakas, J. 2016, ApJ, 830, 4
- Curti, M., D'Eugenio, F., Carniani, S., et al. 2023, MNRAS, 518, 425, doi: 10.1093/mnras/stac2737
- de Mello, D. F., Leitherer, C., & Heckman, T. M. 2000, ApJ, 530, 251, doi: 10.1086/308358
- Ekström, S., Georgy, C., Eggenberger, P., et al. 2012, A&A, 537, A146, doi: 10.1051/0004-6361/201117751
- Eldridge, J. J., Stanway, E. R., Xiao, L., McClelland, L. A. S., & others. 2017, PASA, 34, e058, doi: 10.1017/pasa.2017.51
- Esteban, C., Bresolin, F., García-Rojas, J., & Toribio San Cipriano, L. 2020, MNRAS, 491, 2137, doi: 10.1093/mnras/stz3134
- Esteban, C., Bresolin, F., Peimbert, M., et al. 2009, ApJ, 700, 654
- Esteban, C., García-Rojas, J., Carigi, L., et al. 2014, MNRAS, 443, 624
- Esteban, C., Peimbert, M., Torres-Peimbert, S., & Escalante, V. 1998, MNRAS, 295, 401,
 - doi: 10.1046/j.1365-8711.1998.01335.x
- Ferland, G. J., Porter, R. L., van Hoof, P. A. M., & others. 2013, RMxAA, 49, 137
- Ferrarese, L., Ford, H. C., Huchra, J., et al. 2000, ApJS, 128, 431, doi: 10.1086/313391
- García-Benito, R., Pérez, E., Díaz, Á. I., Maíz Apellániz, J., & Cerviño, M. 2011, AJ, 141, 126, doi: 10.1088/0004-6256/141/4/126
- Garnett, D. R., Shields, G. A., Peimbert, M., et al. 1999, ApJ, 513, 168, doi: 10.1086/306860
- Garnett, D. R., Skillman, E. D., Dufour, R. J., et al. 1995, ApJ, 443, 64
- Gräfener, G., & Hamann, W. R. 2008, A&A, 482, 945, doi: 10.1051/0004-6361:20066176
- Green, G. 2018, The Journal of Open Source Software, 3, 695, doi: 10.21105/joss.00695
- Groh, J. H., Meynet, G., Ekström, S., & Georgy, C. 2014, A&A, 564, A30, doi: 10.1051/0004-6361/201322573
- Harris, C. R., Millman, K. J., van der Walt, S. J., et al. 2020, Nature, 585, 357, doi: 10.1038/s41586-020-2649-2

Henry, R. B. C., Edmunds, M. G., & Köppen, J. 2000, ApJ, 541, 660

- Hill, J. M., Green, R. F., Ashby, D. S., et al. 2010, in Society of Photo-Optical Instrumentation Engineers (SPIE) Conference Series, Vol. 7733, Ground-based and Airborne Telescopes III, 77330C, doi: 10.1117/12.856479
- Hodge, P. W., Gurwell, M., Goldader, J. D., & Kennicutt, Robert C., J. 1990, ApJS, 73, 661, doi: 10.1086/191483
- Jenkins, E. B. 2009, ApJ, 700, 1299
- —. 2014, ArXiv e-prints. https://arxiv.org/abs/1402.4765
- Kelly, B. C. 2007, ApJ, 665, 1489
- Kennicutt, R. C., Calzetti, D., Aniano, G., et al. 2011, PASP, 123, 1347
- Kluyver, T., Ragan-Kelley, B., Pérez, F., et al. 2016, in Positioning and Power in Academic Publishing: Players, Agents and Agendas, ed. F. Loizides & B. Schmidt, IOS Press, 87 – 90
- Kobayashi, C., & Ferrara, A. 2024, ApJL, 962, L6, doi: 10.3847/2041-8213/ad1de1
- Lamers, H. J. G. L. M., Haser, S., de Koter, A., & Leitherer, C. 1999, ApJ, 516, 872, doi: 10.1086/307127
- Leitherer, C., Byler, N., Lee, J. C., & Levesque, E. M. 2018, ApJ, 865, 55, doi: 10.3847/1538-4357/aada84
- Leitherer, C., Ekström, S., Meynet, G., et al. 2014, ApJS, 212, 14, doi: 10.1088/0067-0049/212/1/14
- Leitherer, C., & Heckman, T. M. 1995, ApJS, 96, 9, doi: 10.1086/192112
- Leitherer, C., Schaerer, D., Goldader, J. D., et al. 1999, ApJS, 123, 3
- Leitherer, C., Tremonti, C. A., Heckman, T. M., & Calzetti, D. 2011, AJ, 141, 37
- Luridiana, V., Morisset, C., & Shaw, R. A. 2015, A&A, 573, A42
 Maiolino, R., Scholtz, J., Witstok, J., Carniani, S., et al. 2023,
 arXiv e-prints, arXiv:2305.12492,
 doi: 10.48550/arXiv.2305.12492
- Markwardt, C. B. 2009, in Astronomical Society of the Pacific Conference Series, Vol. 411, Astronomical Data Analysis Software and Systems XVIII, ed. D. A. Bohlender, D. Durand, & P. Dowler, 251
- Martins, F., Hillier, D. J., Paumard, T., et al. 2008, A&A, 478, 219, doi: 10.1051/0004-6361:20078469
- Martins, F., & Palacios, A. 2022, A&A, 659, A163, doi: 10.1051/0004-6361/202243048
- Martins, F., Schaerer, D., Marques-Chaves, R., & Upadhyaya, A. 2023, A&A, 678, A159, doi: 10.1051/0004-6361/202346732
- Maseda, M. V., Lewis, Z., Matthee, J., et al. 2023, ApJ, 956, 11, doi: 10.3847/1538-4357/acf12b
- Matsuoka, K., Nagao, T., Maiolino, R., et al. 2017, A&A, 608, A90, doi: 10.1051/0004-6361/201629878
- Meynet, G., Maeder, A., Schaller, G., Schaerer, D., & Charbonnel, C. 1994, A&AS, 103, 97

- Nakajima, K., Ouchi, M., Isobe, Y., et al. 2023, ApJS, 269, 33, doi: 10.3847/1538-4365/acd556
- Neustadt, J. M. M., Kochanek, C. S., Stanek, K. Z., et al. 2021, MNRAS, 508, 516, doi: 10.1093/mnras/stab2605
- Newville, M., Otten, R., Nelson, A., et al. 2018, lmfit/lmfit-py 0.9.12, 0.9.12, Zenodo, Zenodo, doi: 10.5281/zenodo.1699739
- Nicholls, D. C., Sutherland, R. S., Dopita, M. A., Kewley, L. J., & Groves, B. A. 2017, MNRAS, 466, 4403
- Peimbert, A., & Peimbert, M. 2010, ApJ, 724, 791
- Peimbert, A., Peimbert, M., & Ruiz, M. T. 2005, ApJ, 634, 1056
- Pogge, R. W., Atwood, B., Brewer, D. F., et al. 2010, in Society of Photo-Optical Instrumentation Engineers (SPIE) Conference Series, Vol. 7735, Society of Photo-Optical Instrumentation Engineers (SPIE) Conference Series
- Reddy, N. A., Steidel, C. C., Pettini, M., Bogosavljević, M., & Shapley, A. E. 2016, ApJ, 828, 108, doi: 10.3847/0004-637X/828/2/108
- Rogers, N. S. J., Strom, A. L., Rudie, G. C., et al. 2023, arXiv e-prints, arXiv:2312.08427, doi: 10.48550/arXiv.2312.08427
- Sander, A., Shenar, T., Hainich, R., et al. 2015, A&A, 577, A13, doi: 10.1051/0004-6361/201425356
- Schaerer, D., & Vacca, W. D. 1998, ApJ, 497, 618
- Senchyna, P., Plat, A., Stark, D. P., & Rudie, G. C. 2023, arXiv e-prints, arXiv:2303.04179, doi: 10.48550/arXiv.2303.04179
- Senchyna, P., Stark, D. P., Vidal-García, A., et al. 2017, MNRAS, 472, 2608
- Sirressi, M., Adamo, A., Hayes, M., et al. 2022, AJ, 164, 208, doi: 10.3847/1538-3881/ac9311

- Skillman, E. D., Berg, D. A., Pogge, R. W., et al. 2020, ApJ, 894, 138, doi: 10.3847/1538-4357/ab86ae
- Smith, L. F., Shara, M. M., & Moffat, A. F. J. 1996, MNRAS, 281, 163, doi: 10.1093/mnras/281.1.163
- Smith, L. J., Crowther, P. A., Calzetti, D., & Sidoli, F. 2016, ApJ, 823, 38, doi: 10.3847/0004-637X/823/1/38
- Stanway, E. R., & Eldridge, J. J. 2018, MNRAS, 479, 75, doi: 10.1093/mnras/sty1353
- Todt, H., Sander, A., Hainich, R., et al. 2015, A&A, 579, A75, doi: 10.1051/0004-6361/201526253
- Toribio San Cipriano, L., Domínguez-Guzmán, G., Esteban, C., et al. 2017, MNRAS, 467, 3759, doi: 10.1093/mnras/stx328
- Toribio San Cipriano, L., García-Rojas, J., Esteban, C., Bresolin, F., & Peimbert, M. 2016, MNRAS, 458, 1866, doi: 10.1093/mnras/stw397
- Tumlinson, J., Shull, J. M., Rachford, B. L., et al. 2002, ApJ, 566, 857, doi: 10.1086/338112
- Virtanen, P., Gommers, R., Oliphant, T. E., et al. 2020, Nature Methods, 17, 261, doi: 10.1038/s41592-019-0686-2
- Vogt, S. S., Allen, S. L., Bigelow, B. C., et al. 1994, in Society of Photo-Optical Instrumentation Engineers (SPIE) Conference Series, Vol. 2198, Instrumentation in Astronomy VIII, ed. D. L. Crawford & E. R. Craine, 362, doi: 10.1117/12.176725
- Walter, F., Brinks, E., de Blok, W. J. G., et al. 2008, AJ, 136, 2563, doi: 10.1088/0004-6256/136/6/2563
- Willis, A. J., Crowther, P. A., Fullerton, A. W., et al. 2004, ApJS, 154, 651, doi: 10.1086/422825